ARTICLE

Genesis of Devonian volcanic-associated Lahn-Dill-type iron ores — part I: iron mobilisation and mineralisation style

Leanne Schmitt[1,2] · Thomas Kirnbauer[1] · Thomas Angerer[3] · Rebecca Volkmann[1,4] · Vladimir Roddatis[4] · Richard Wirth[4] · Sabine Klein[1,5]

Abstract

Fe-oxide deposits of the Lahn-Dill-type in the eastern Rhenish Massif comprise haematite and quartz with minor siderite, magnetite, and calcite. The deposits are located in the hanging wall of thick volcaniclastic rock sequences and mark the Middle to Late Devonian boundary. Varying ore types with accompanying footwall rocks were sampled from two formerly important ore deposits, the Fortuna mine (Lahn syncline) and the Briloner Eisenberg mine (East Sauerland anticline), in order to elucidate the interplay of processes leading to ore formation. Deposit geology, petrography, and whole-rock geochemistry suggest that the ores formed by iron mobilisation from deeply altered footwall volcaniclastic rocks, subsequent venting of a modified H_2O-CO_2-Fe-rich and H_2S-poor fluid, and precipitation on the seafloor (sedimentary-type), or locally by metasomatic replacement of wall rocks (replacement-type). Petrographic analysis to the sub-micron scale revealed that the sedimentary-type ores most likely formed from a Fe-Si-rich gel and accompanying maturation. Early gel textures include the presence of spherules, aggregates, tubes, and filamentous stalks consisting of nanocrystalline haematite dispersed in a matrix of microcrystalline quartz. Local diagenetic Fe^{3+} reduction within the gel is indicated by siderite replacement of haematite. Replacement-type ores formed due to a two-step process including coprecipitation of (precursor) haematite and carbonates and subsequent metasomatic replacement by haematite. These ore-forming processes took place during a time when several restricted shallow marine basins in the north-eastern Rheic Ocean were influenced by extensive volcanism and associated hydrothermal fluid flux. Examples of similar volcanic-associated Fe-oxide occurrences of Silurian to Carboniferous age can be categorised as being of Lahn-Dill-type ores as well.

Keywords Iron ore · Chemical sediment · Gel formation · Rhenish Massif · Wall rock metasomatism · Microbial

✉ Leanne Schmitt
leanne.schmitt@ruhr-uni-bochum.de

1 Institute of Geology, Mineralogy and Geophysics, Ruhr University Bochum, 44801 Bochum, Germany

2 Faculty of Georesources and Process Engineering, Technische Hochschule Georg Agricola, Herner Straße 45, 44787 Bochum, Germany

3 Department of Mineral Resources and Geoenergy, GeoSphere Austria, 1190 Vienna, Austria

4 GFZ German Research Centre for Geosciences, 14473 Potsdam, Germany

5 Deutsches Bergbau-Museum Bochum, 44791 Bochum, Germany

Introduction

Lahn-Dill-type iron ores are here defined as marine volcanic-associated Fe-oxide (typically haematite) deposits that formed at the Middle to Late Devonian boundary in restricted, shallow marine basins associated with mafic volcanism. They do not share similarities with the most common iron ore deposits — ooidal ironstones — in the Phanerozoic (Bekker et al. 2010), as Lahn-Dill-type iron ores do not contain ooids but are characterised by abundant quartz (cf. Petránek and van Houten 1997; Di Bella et al. 2019). Lahn-Dill-type iron ores, however, share similarities with Precambrian iron formation of the Algoma-type, several Palaeozoic Fe-oxide occurrences, and modern Fe-Si-rich vent deposits (Kräutner 1977; Gross 1980; Kimberley 1989; Duhig et al. 1992; Grenne and Slack 2003a; Edwards et al. 2011; González et al. 2020).

These deposits and occurrences are usually interpreted to have formed due to an interplay of hydrothermal, marine, microbial, and (post-)depositional processes and therefore represent important archives and provide palaeoproxies for basin sedimentation and marine environmental conditions (Grenne and Slack 2003b; Bekker et al. 2010; Kendall et al. 2012). In addition to their value as recorders of past submarine systems, Lahn-Dill-type iron ore deposits have been significant sources of iron.

The ore mineralogy of Lahn-Dill-type iron ores is dominated by Fe-oxides, with far more haematite than magnetite, and minor siderite, and a gangue dominated by quartz and minor calcite (Quade 1968). Primary to diagenetic textures include (1) quartz-haematite spherules surrounded by cracks that formed due to shrinkage, (2) aggregates of haematite dispersed in quartz, and (3) aggregates of fine-crystalline haematite (Cissarz 1924; Harder 1954; Quade 1968). These textures are typically well preserved due to (very) low-grade metamorphic overprints ($T < 300$ °C; Meisl 1970). Their common occurrence in many other types of volcanic-associated Fe-oxide deposits is interpreted as evidence of coprecipitation of colloidal Fe-(oxyhydr)oxides and silica forming a Si-Fe-rich gel (Duhig et al. 1992; Grenne and Slack 2003a; Egglseder et al. 2018; Abd El-Rahman et al. 2019). Preservation of primary features in Lahn-Dill-type iron ores makes such deposits favourable for studying mineralogical and textural changes from early diagenesis to low-grade metamorphism.

Lahn-Dill-type iron ores were mined for over a thousand years, and therefore, a significant volume of research output has accumulated during the twentieth century leading to numerous proposed genetic models. However, despite this extensive research, many uncertainties remain regarding (1) fluid source and composition, (2) venting mechanisms, and (3) depositional processes from Fe-Si-rich gel to ore, including modes of Fe-(oxyhydr)oxide and silica transformation during diagenetic gel maturation and related textural changes. Processes involved in the metasomatic replacement of wall rocks as part of Lahn-Dill-type iron ore formation have essentially been unaddressed for the last 170 years.

Here, we present new data for Lahn-Dill-type iron ores, applying a systematic approach using optical microscopy, scanning and transmission electron microscopy (SEM, TEM), and whole-rock chemical analysis of underlying wall rocks. One of the largest Lahn-Dill-type iron ore mines (Fortuna) and the smaller Briloner Eisenberg mine were the focus of our studies. Representative profiles of footwall volcaniclastic rocks (the proposed metal source) and ores were mapped, detailed high-resolution petrography was done on ore samples, and geochemical data were acquired on footwall rocks. These studies are designed to address the above questions as well as to decipher the (hydrothermal) Fe pathway from source rock (mobilisation) to ore sink (deposition).

A detailed geochemical study of the Fortuna deposit will be presented in a companionable paper (Schmitt et al. n.d).

Lahn-Dill-type iron ores in the Rhenish Massif

Central Europe hosts stratiform submarine volcanic-associated Fe-oxide deposits known as "Lahn-Dill-type" (Ahlburg 1911). Type localities are the Lahn and Dill synclines in the eastern Rhenish Massif of Germany, which is part of the Rhenohercynian Zone of the Variscan Orogen (Fig. 1a, b). Lahn-Dill-type iron ores also occur in other parts of the Rhenohercynian Zone (Fig. 1a), including the East Sauerland anticline (Fig. 1c) and the Harz Mountains (Oberharzer diabase zone, Elbingeröder Complex; all in Germany). Other Lahn-Dill-type ore deposits were mined in the central Saxothuringian Zone (Fig. 1a; Bergaer anticline, SW Thuringian-Vogtland syncline; Germany) and the eastern Sudetes (Moravo-Silesion Zone; Czech Republic). In all of these localities, the ores display a close stratigraphic relation to volcanic and volcaniclastic rocks (named "Schalstein" by local miners in the Lahn-Dill district) that were deposited near the Middle to Late Devonian boundary (Roemer 1844; Ahlburg 1911).

The iron ores formed in relation to two different mineralising processes: chemical precipitation on the seafloor (termed sedimentary-type) and wall rock metasomatism (termed replacement-type). Sedimentary- and replacement-type ores occur in three different lithostratigraphic positions (positions A to C). These include ores intercalated with footwall volcanic and volcaniclastic rocks (position A) forming layers and lenses ranging in thickness from several centimetres to a few metres (Bottke 1965; Quade 1968). Locally, in position A, volcaniclastic rocks and pillow basalt were metasomatically replaced by haematite (Lippert 1951). The main ore zone in terms of thickness, extension, and grade is located directly on top of thick volcaniclastic successions (position B). Position B ores reach thicknesses of > 10 m and lateral extent of up to 1 km (Lippert 1997). These ores form massive and rarely bedded stratiform layers and lenses (Lippert 1953) or metasomatic replacement bodies in limestone (Roemer 1844; Kegel 1922) and in volcanic and volcaniclastic rocks (Lippert 1953). Position C ores form thin (< 3 m) layers and lenses, which are intercalated with Upper Devonian hanging wall volcano-sedimentary rocks, or occur as replacements of wall rocks as well as re-sedimented breccias (Krebs 1960).

Typically, Lahn-Dill-type iron ores average 30 to 40 wt% Fe and comprise haematite with varying amounts of quartz, calcite, siderite, and magnetite (Quade 1968; Lippert 1997). Lateral and vertical zonations are documented from quartz-rich to haematite-rich to carbonate-rich ores with increasing distance to vent sites and carbonate enrichment towards the top of the ore bodies (Lippert 1951). Locally preserved ores

Fig. 1 Geological overview of Lahn-Dill-type iron ores and sampled mines. **a** Outline of Germany showing selected outcrops of Variscan Massifs and areas with Lahn-Dill-type iron ores (red) restricted to the Rhenohercynian Zone (1, Lahn syncline; 2, Dill syncline; 3, East Sauerland anticline; 4, Oberharzer diabase zone; 5, Elbingeröder Complex) and central Saxothuringian Zone (6, Bergaer anticline; 7, Thuringian-Vogtland syncline). **b** Geological map of the north-eastern Lahn syncline dominated by volcaniclastic rocks forming the "Schalsteinhauptzug" and showing location of the Fortuna mine (modified after Kegel 1922). **c** Geological map of the East Sauerland anticline with location of the Briloner Eisenberg mine (modified after HLNUG 2007). **d** Cross-section of the Fortuna mine showing the heavily dissected and folded western and eastern ore bodies; black square marks approximate sample location on the 150-m level (modified after Dengler 1963). **e** Map of the Briloner Eisenberg mine depicting dissected ore body; black square marks approximate sample location on the Philippstollen level (modified after Castendyk 1855)
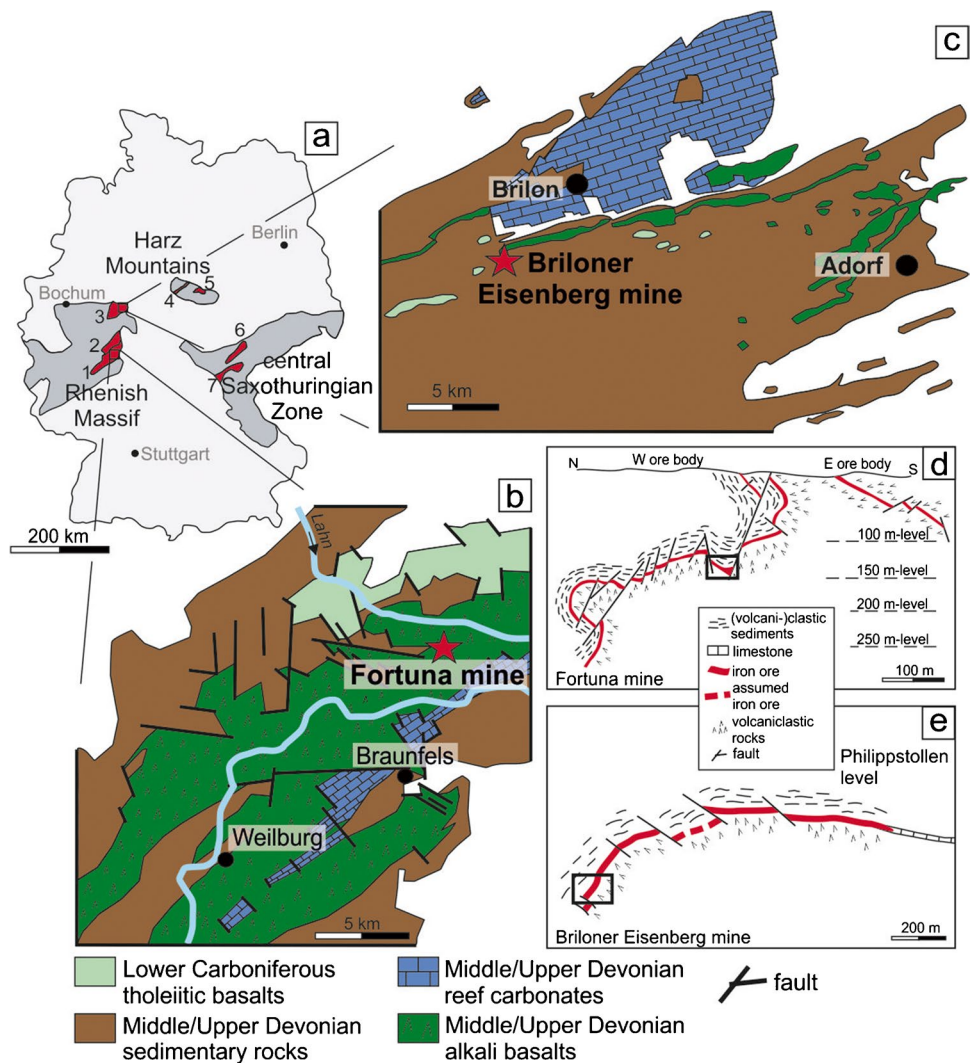
containing siderite, magnetite, pyrite, or chamosite as main constituents have been interpreted as primary depositional facies (Bottke 1965; Quade 1968). Many genetic models have been discussed during the last 160 years. One of the first published concepts involved epigenetic replacement of wall rocks related to iron mobilisation from surrounding rocks and subsequent iron oxidation (Sandberger 1847). Decades later, von Gümbel (1879) and others proposed a syngenetic origin in close relation to marine volcanic processes. With the discovery of crescent-shaped cracks interpreted as textures related to shrinkage by Cissarz (1924), most of the geological community accepted Lahn-Dill-type iron ores as primary precipitates that formed from a hydrous gel on the seafloor. Volcanogenic iron was believed to be transported by hydrothermal waters or vapours driven by a volcanogenic heat source (Quade 1968). Alternative models have invoked the mobilisation of iron from footwall volcanic and volcaniclastic rocks by diagenetic fluids (Flick et al. 1990).

Tectonostratigraphic setting

Throughout the Early Devonian, shallow marine basins formed in the north-eastern Rheic Ocean south of the Old Red Continent (Stets and Schäfer 2002; Franke et al. 2017). The formation of these basins was likely triggered by subduction of the Rheic mid-ocean ridge including the opening of the Rhenohercynian Basin (Franke et al. 2017). The Rhenohercynian Basin was a narrow, shallow (< 200 m), and likely restricted back-arc basin that covered the southern shelf of the Old Red Continent (Stets and Schäfer 2002; Nesbor 2004; Franke et al. 2017, 2021). Rift-related crustal extension within the Rhenohercynian Basin resulted in two major intraplate volcanic cycles that culminated during the Givetian/Frasnian and Tournaisian/Visean (Nesbor 2004). Givetian/Frasnian volcanic activity was dominated by the formation of alkali basaltic to basanitic volcanic and volcaniclastic rocks and minor rhyolite and trachyte (Nesbor 2004). Givetian/Frasnian volcanic rocks comprise pillow basalt and

lava flows, whereas the volcaniclastic rocks (main volcanic product) are characterised by lapilli and ash tuffs, pillow breccias, and hyaloclastites (Nesbor et al. 1993). Lower Carboniferous volcanic rocks have a tholeiitic composition (Nesbor et al. 1993).

During Middle to Late Devonian time, a vivid seafloor relief developed within the Rhenohercynian Basin due to the formation of numerous volcanic edifices and basins ranging from a few metres to several kilometres associated with protracted extensional processes (Krebs 1960). In times of volcanic quiescence, reef growth was facilitated on volcanic ridges and iron ores formed on volcanic flanks (Bottke 1965). Receding volcanic activity and subsequent rapid erosion of volcanic edifices, reefs, and iron ores yielded small-scale facies changes of related volcaniclastic and sedimentary rocks (Lippert 1951; Krebs 1960). Consequently, during the Late Devonian, a short-lived and diverse environment arose leading to rapid alternations of tuff, clastic sediment, limestone, iron ore, and accompanying breccias (Krebs 1960).

The above-described Palaeozoic successions were subsequently deformed by folds and thrust faults during the Variscan collision of Gondwana with the Old Red Continent (Franke 1989; Franke et al. 2021). Orogeny-associated NE-SW-trending tectonic structures formed due to major compressional processes (Franke 1989). NW–SE shortening accounted for at least 40% of the original width, which led to the formation of synclines and anticlines including the Lahn and Dill synclines (Dittmar et al. 1994). Accompanying metamorphism ranged from prehnite-pumpellyite to lower greenschist facies with temperatures below 300 °C in the Rhenish Massif (Meisl 1970).

Ore deposit geology

Fortuna mine

The Lahn and Dill synclines host numerous small ore deposits rarely exceeding 5 Mt but with exceptions containing up to 10 Mt of ore averaging 30 to 40 wt% Fe (Quade 1968; Lippert 1997). The Fortuna mine was one of the economically most important Lahn-Dill-type iron ore mines with 4.7 Mt of mined ore averaging ca. 40 wt% Fe and 3.8 Mt of remaining reserves (Dengler 1963; Quade 1969). The mine is located 7 km north of Braunfels within the northern Lahn syncline (Fig. 1b). This NE-SW-striking syncline mainly comprises Middle to Upper Devonian clastic sedimentary rocks, and Givetian/Frasnian volcanic and volcaniclastic rocks forming the "Schalsteinhauptzug," and locally intercalated limestone (Kegel 1922). According to Quade (1968), ores of the Fortuna mine formed near a volcanic centre.

The Fortuna mine stratigraphy is characterised by footwall volcaniclastic rocks, position A to C ores, and hanging wall clastic sedimentary rocks (Quade 1968; Quade et al. 1981). The volcaniclastic succession can reach thicknesses of at least 150 m in which the rocks are commonly green but change to purple towards the ore (Saffarini 1982). A NNE-SSW-striking fault separates the Fortuna mine ores into western and eastern ore bodies (Fig. 1d) with the former being economically more important (Quade 1968). The eastern ore body contains position A ores with a thickness of averaging 2 m intercalated with volcaniclastic rocks (Dengler 1963). The main western ore body is located on top of the volcaniclastic succession and is up to 14 m thick (Quade 1968). It strikes SW-NE over a length of ~ 1200 m and is strongly dissected by steep normal and shallow thrust faults (Quade 1968), the latter leading to a complexly stacked stratigraphy (Fig. 1d). Position C ores only occur to a minor extent within the Fortuna mine, reaching up to 1 m in thickness and are intercalated with clastic and volcaniclastic rocks and limestone (Dengler 1963; Quade 1968).

Briloner Eisenberg mine

The Briloner Eisenberg mine is located in the north-eastern Rhenish Massif within the eastern Sauerland (Fig. 1c). The eastern Sauerland is characterised by a major anticline (East Sauerland anticline) that mainly comprises Middle to Upper Devonian clastic sedimentary rocks (Bottke 1965). Covering its northern and southern anticlinal limbs, volcanic and volcaniclastic rocks with locally intercalated (bituminous) limestone formed successions reaching thicknesses of up to 250 m (Bottke 1965). Hanging wall strata overlying the volcanic and volcaniclastic rocks comprise clastic sedimentary rocks and limestone (Bottke 1965). Located at the north-western anticlinal limb, the Briloner Eisenberg mine is arrayed with other Lahn-Dill-type iron ore deposits forming a half circle around the East Sauerland anticline (Bottke 1965). Iron ores occur as small bodies (100,000 t to 3 Mt) on top of volcanic and volcaniclastic successions, as stratiform sedimentary-type ore layers and replacement-type ore lenses within limestone (Bottke 1965).

Stratigraphy within the Briloner Eisenberg mine is characterised by volcaniclastic rocks forming a succession of approximately 200 m (Castendyk 1855). Position B ores occur in the structural footwall of overthrust volcaniclastic rocks (Castendyk 1855). Stratigraphic units dip steeply towards the south (Castendyk 1855). Ore bodies partially grade laterally into limestone and shale (Castendyk 1855). Position A and C ores are absent in this mine (Castendyk 1855).

Field relations and sampling

We sampled part of the western Fortuna mine ore body on the 150-m level (Fig. 1d). There, the stratigraphy comprises a 136-m-thick sequence of volcaniclastic rocks with intercalated position A ores at the top and overlying position B ores (Fig. 2a). The volcaniclastic sequence mainly consists of green volcaniclastic rocks, but purple volcaniclastic rocks account for the upper 18 m of the sequence. Position A ores are represented by several thin (0.1–0.5 m) ore lenses that are locally cut by W-E striking faults and show a sharp contact with footwall and hanging wall rocks (Fig. 2b). The position B ore body reaches a maximum thickness of 5 m (Fig. 2c) and pinches out without tectonic restriction. The contact between position B ore and footwall rocks is sharp, whereas hanging wall rocks are gradually intercalated at the top. The entire stratigraphic succession is cut by numerous hydrothermal carbonate-quartz ± haematite (syn-Variscan) and carbonate-quartz-chlorite ± haematite ± apatite (late-Variscan) veins (Kirnbauer 1998). Additionally, the volcaniclastic rocks are cut by faults spatially associated with bleaching and small haematite-rich veinlets.

In the Fortuna mine, volcaniclastic rocks were sampled in 5 to 10 m intervals starting as close to the ore layer as possible. Sampled volcaniclastic rocks ($n = 17$) include green ($n = 11$) and purple ($n = 6$) varieties. Four ore samples were collected from two different position A lenses. Position B ores were sampled in 0.3 to 0.5 m intervals across the 5-m-thick ore layer ($n = 14$). Position C ores could not be sampled due to an inaccessible location. Sampled ores in positions A and B in the Fortuna mine have been interpreted as sedimentary-type ores. Based on mineralogical composition, they can be characterised as haematite-quartz and siderite-haematite ores (Figs. 3 and 4). Position A ore lenses consist of haematite-quartz ores, whereas position B ores are dominated by haematite-quartz, and minor siderite-haematite ores, which occur at the top of the ore body.

Ores were also sampled from the Philippstollen level in the Briloner Eisenberg mine (Fig. 1e). Stratigraphic units there comprise footwall volcaniclastic rocks with a position B ore body on top and stratigraphic hanging wall rocks dominated by dolostone (Fig. 2d). The volcaniclastic succession consists mainly of green volcaniclastic rocks turning purple towards the ore. Thicknesses of the position B ore body increase from 2.8 to 3.4 m along strike (Fig. 2e). A fault separates the position B ore body and footwall volcaniclastic rocks. Ores were sampled in 0.3 to 1 m intervals covering the entire thickness of the ore body. These samples are identified mainly as replacement-type calcite-haematite ores occurring heterogeneously in
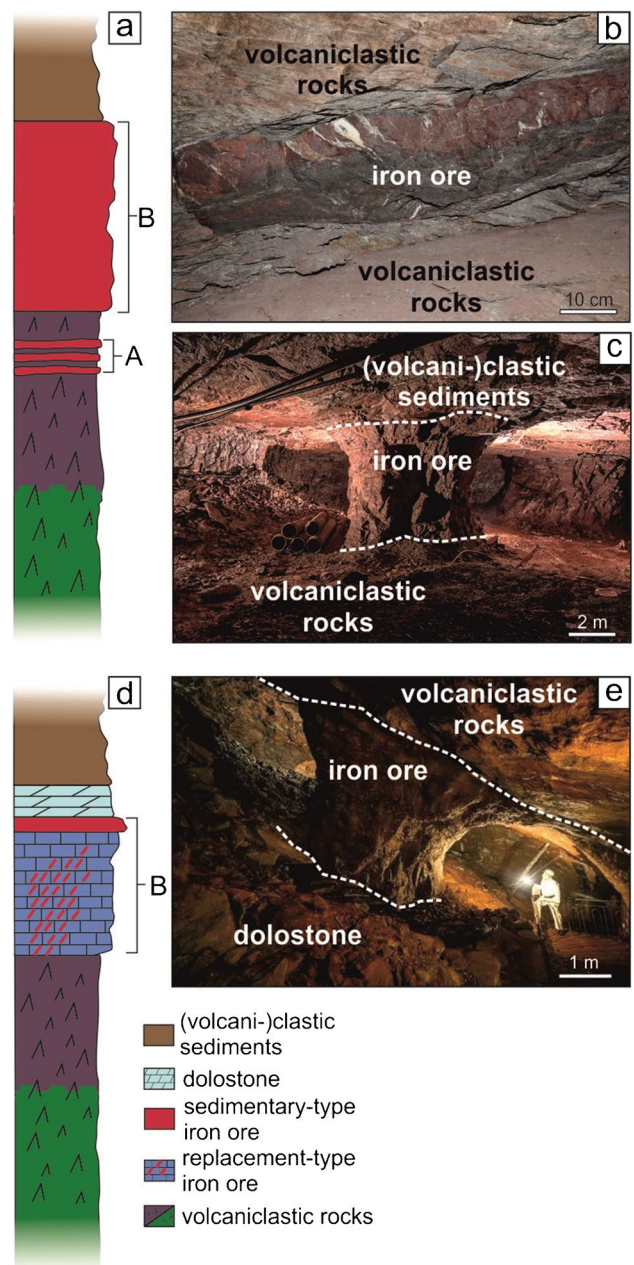

Fig. 2 Schematic lithostratigraphic column of sampled areas in the Fortuna and Briloner Eisenberg mines. **a** At least three ore lenses occur intercalated with purple volcaniclastic rocks (position A) in the Fortuna mine. Main ore body (position B) comprises sedimentary-type ores. At the upper contact to hanging wall rocks, ores are partially intercalated with clastic sedimentary rocks. Note that depicted thicknesses of drawn stratigraphic units do not correspond to true thicknesses. For true thicknesses the reader is referred to section "field relations and sampling". **b**, **c** Images of position A ores **b** and position B ores in the Fortuna mine (**c**; image by courtesy of Roger Lang/Geowelt Fortuna e.V). **d** Schematic lithostratigraphy of the Briloner Eisenberg mine in which ores only occur at position B. Ore layer comprises sedimentary- and replacement-type ores. **e** Overthrust lithostratigraphy of position B ore body in the Briloner Eisenberg mine (image by courtesy of Klaus-Peter Kappest/Tourismus Brilon Olsberg GmbH)
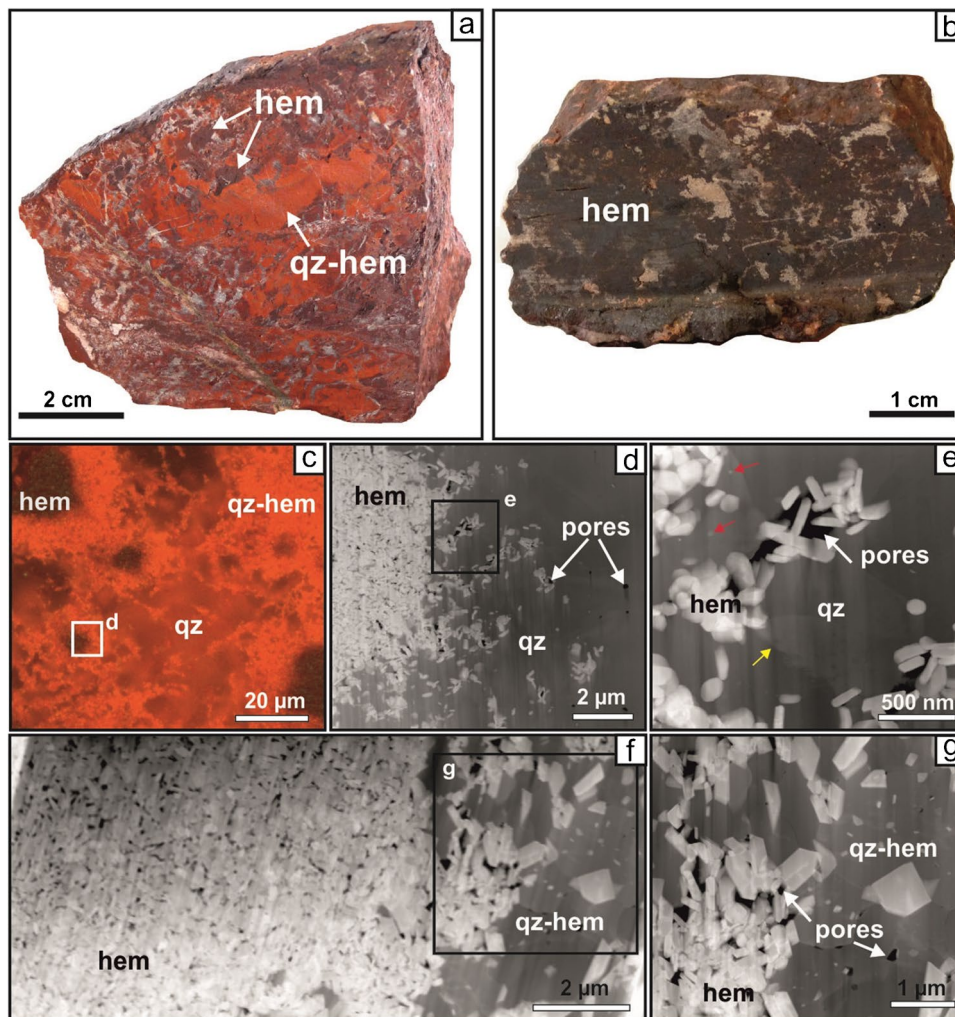
Fig. 3 Petrographic images of sedimentary-type haematite-quartz ores from the Fortuna mine (**a** position B, sample DLFo008) and Briloner Eisenberg mine (**b** position B, sample DSEb011). **c** Quartz-haematite microdomain surrounding haematite microdomain spherules in quartz microdomain matrix. **d** Haematite microdomain surrounded by porous quartz microdomain grain. **e** Haematite microdomain accumulated in quartz microdomain pores. Red arrows indicate nanocrystalline haematite remnants in quartz. Subgrain formation in quartz is visible (yellow arrow). **f** Interface between haematite to quartz-haematite microdomains. Haematite microdomain shows varying intergranular porosity. **g** Haematite microdomain associated with pores in quartz-haematite microdomain. A size difference between haematite in haematite and quartz-haematite microdomains is present. **h** Quartz-haematite microdomain spherules within haematite microdomain aggregates. Spherules are surrounded by crescent-shaped cracks. **i** Haematite microdomain aggregates surrounded by quartz-haematite microdomain aggregates. Interstices are filled by quartz microdomains. **j** Tube and filamentous stalk-like textures formed by quartz-haematite microdomains. **k** Chalcedony relics (two marked) with dispersed haematite exceeding quartz grain boundaries. **c, i–k** = reflected light photomicrographs, **d–g** = STEM HAADF images, **h** = BSE SEM image. qz-hem, quartz-haematite microdomain; hem, haematite microdomain; qz, quartz microdomain (hem, haematite; qz, quartz)

limestone and minor sedimentary-type haematite-quartz ores forming a thin (~ 15 cm) layer between the replaced limestone and hanging wall dolostone. Samples comprise (1) four replacement-type calcite-haematite ores, (2) three unmineralised limestones, (3) one sedimentary-type haematite-quartz ore, and (4) one hanging wall dolostone sample. Footwall volcaniclastic rocks were not sampled within the Briloner Eisenberg mine due to poor accessibility.

In both mines, obvious fault zones as well as strongly tectonically deformed wall rocks and ores were avoided during sampling. Table SM1 in the online supplementary material presents a list of all samples with relevant characteristics.

Analytical methods

Petrographic studies of ores and volcaniclastic rocks were conducted using a Zeiss Axiophot transmission and reflected light microscopy and a Zeiss SUPRA 40 VP scanning electron microscope (SEM) at the Deutsches Bergbau-Museum
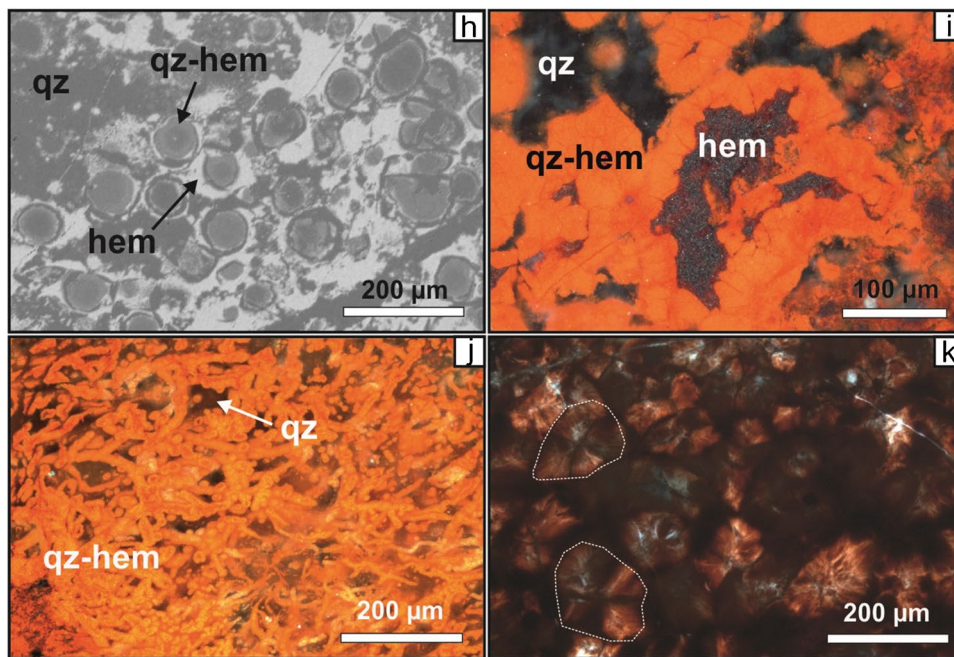
Fig. 3 (continued)

Bochum. Back-scattered electron (BSE) imaging and energy-dispersive X-ray spectrometry (EDS) were performed at 20 kV for documenting textures and obtaining semi-quantitative mineral compositions, respectively. Transmission electron microscopy (TEM) was carried out using Thermo Fisher Scientific (former FEI) Tecnai F20 G2 and Themis Z 80–300 microscopes operated at 200 kV and 300 kV, respectively. Specimens for TEM were prepared by the lift-out technique using a Thermo Fisher Scientific (former FEI) Helios G4UC dual-beam instrument. The specimens were cut out using a Ga$^+$ ion beam with an energy of 30 kV and were further thinned using 16 kV. The final polishing was performed at 5 kV.

For whole-rock major, minor, and trace element analyses of sampled footwall volcaniclastic rocks, ~500 g of sample material was crushed in a steel crusher, cleansed with H_2O, and picked to remove weathering surfaces, veins and altered material, and metal fillings from the crusher. Crushed rock chips were powdered and homogenised in an agate mill. Whole-rock major element analysis was conducted using a Rigaku ZSX Primus IV wavelength-dispersive X-ray fluorescence spectrometer (WDXRF) at the Institut für Geologie, Mineralogie und Geophysik at Ruhr-Universität Bochum. Approximately 1 g of rock powder (< 70 µm particle size) was fused with MERCK A12 (di-lithium tetraborate and lithium metaborate) to fusion discs (1:10 sample powder to flux ratio). For further information on calibration, uncertainties, and analysis of volatile components, see online supplementary information 1.

Minor and trace element analysis was conducted on aliquots of the footwall volcaniclastic rock samples using a PerkinElmer NexION 350×low-resolution quadrupole inductively coupled plasma-mass spectrometer (ICP-MS) coupled to an Element Scientific Apex 2 desolvating system at Jacobs University Bremen. Results of multiple analyses of the certified reference material BHVO-2 (Jochum et al. 2005) were used to evaluate precision and accuracy. WDXRF and ICP-MS data are listed in Table SM2 in the online supplementary material, and a detailed description of wet chemical preparation is presented in the online supplementary information 2.

Petrography

Sedimentary-type haematite-quartz ores

Sampled sedimentary-type haematite-quartz ores in the Fortuna (Fig. 3a) and Briloner Eisenberg (Fig. 3b) mines are mineralogically simple (quartz and haematite) but display complex textures. Three different microdomains have been identified based on typical ranges of modal composition and textural relationships of quartz and haematite: quartz-haematite, haematite, and quartz microdomains (Fig. 3; Table 1). These microdomains commonly occur adjacent to each other in all the sampled haematite-quartz ores.

The quartz-haematite microdomains consist of microcrystalline and anhedral quartz (0.5–2 µm) with varying amounts of finely dispersed tabular haematite (< 200 µm; Fig. 3c–k).

Fig. 4 Petrographic images of sedimentary-type siderite-haematite ores from the Fortuna mine (**a**, **b**; position B, samples DLFo028.2 and DLFo007). **c** Nanocrystalline haematite (white) patchily distributed in a single grain of siderite (grey) forming siderite-haematite microdomains. **d** Haematite from haematite microdomain replaced by nanocrystalline siderite. **e** Siderite-haematite microdomain with spherulitic relics. **f** Siderite-magnetite-haematite microdomain comprising siderite (middle grey), granular magnetite (beige), and haematite (white) that display spherulitic distribution. Interstices are filled by quartz (dark grey). **c** BSE SEM image, **d** TEM BF image, **e**, **f** reflected light photomicrographs. hem, haematite microdomain; qz, quartz microdomain; sd-hem, siderite-haematite microdomain; sd-mag-hem, siderite-magnetite-haematite microdomain (hem, haematite; mag, magnetite; qz, quartz; sd, siderite)
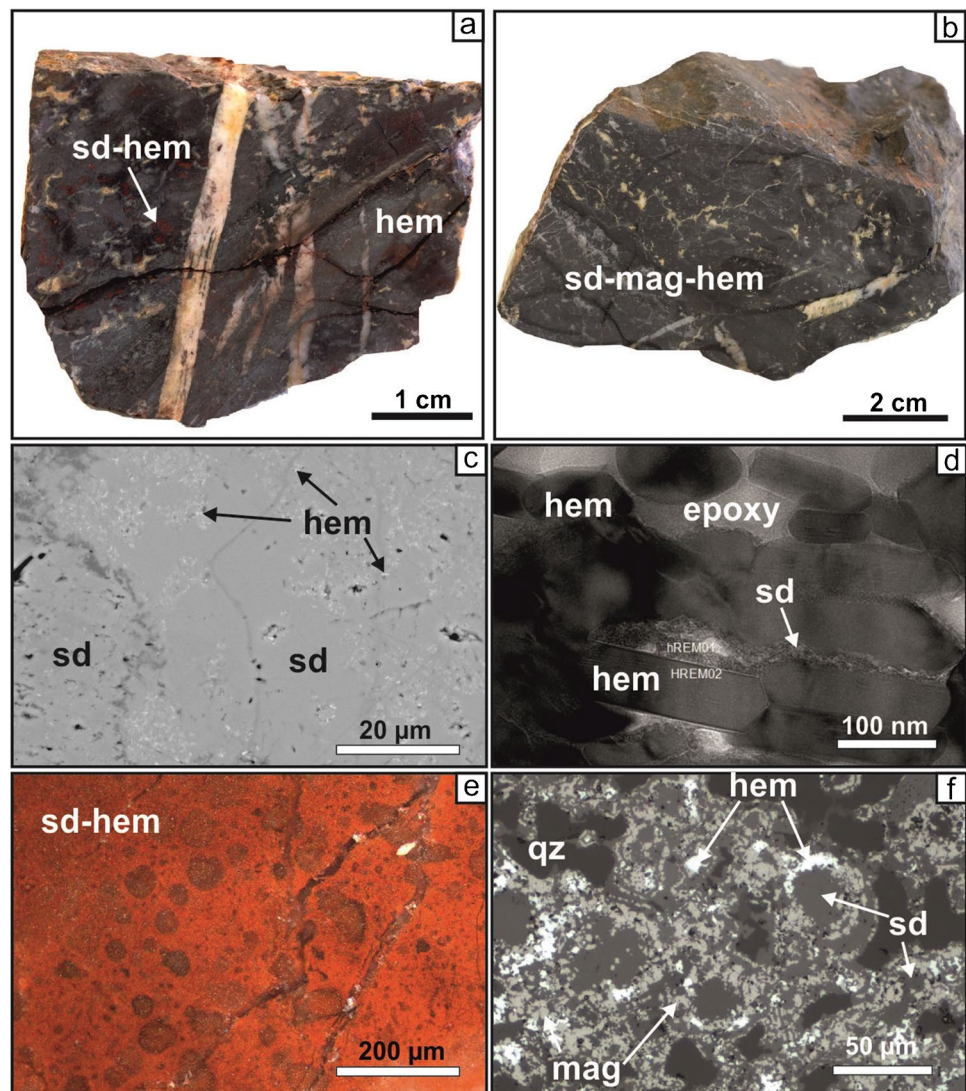
Pores along quartz grain boundaries and within quartz grains are present (Fig. 3d–g). These microdomains of haematite dispersed in quartz are characterised by various types of internal features including spherules, aggregates, and tube and filamentous stalk-like textures. Large spherules (20–80 μm; Fig. 3h) are isolated within haematite aggregates or the quartz matrix, whereas small spherules (5–10 μm) occur in irregularly formed clusters. Spherules are typically centrically zoned with a quartz-rich core and haematite-rich rim and are typically surrounded by crescent-shaped quartz-filled cracks (Fig. 3h). Within the quartz-haematite microdomain aggregates, haematite is heterogeneously distributed across quartz grain boundaries forming irregular clusters (Fig. 3i, k). Tube- and string-like textures include twisted, branching, and coordinated growths imbedded in quartz microdomains (Fig. 3j). In several samples, quartz-haematite microdomain aggregates locally contain relics of radial-symmetric chalcedony (Fig. 3k). The haematite microdomains

comprise nanocrystalline (0.05–1 μm) tabular haematite that appear distinctly larger than haematite in the quartz-haematite microdomains (Fig. 3f, g). Haematite crystals are accumulated with varying abundance with intergranular porosity and can be associated with pores in quartz-haematite and quartz microdomains (Fig. 3d–g). Texturally, the haematite microdomains form aggregates and spherules. Aggregates are typically surrounded by quartz-haematite microdomain aggregates showing either sharp or diffuse contacts (Fig. 3i). Spherules consisting of the haematite microdomain occur isolated in a quartz matrix, range in size from 30 to 300 μm and are commonly surrounded by crescent-shaped cracks. The quartz microdomains comprise microcrystalline quartz (0.5–200 μm), contain abundant pores (Fig. 3d), and generally constitute the matrix and fill "cracks" surrounding the spherules (Fig. 3h). In places, these quartz microdomains occur as deformed veins that cut the quartz-haematite and haematite microdomains.

Table 1 Composition of ores with microdomain characteristics. Mineral abbreviations from Whitney and Evans (2010). For mineral abbreviations, see caption of Fig. 5

	Microdomains in sedimentary-type ores					Microdomains in replacement-type ores	
	Quartz-haematite	Haematite	Quartz	Siderite-haematite	Siderite-magnetite-haematite	Calcite-haematite	Haematite
Mineral relation	Hem dispersed in qz	Accumulated hem crystals	Qz aggregates	Hem dispersed in sd	Mag and hem in sd	Hem dispersed in cc	Hem replacing wall rocks
Crystal shape	Tabular hem anhedral qz	Tabular	Anhedral	Tabular hem anhedral sd	Subhedral mag and hem anhedral sd	Euhedral hem anhedral cc	Euhedral
Crystal size	Qz: 0.5–2 μm; Hem: < 200 nm	50 nm–1 μm	0.5–200 μm	Sd: 0.1–2 mm; Hem: < 500 nm	Sd: 50–200 μm; Mag: 1–5 μm; Hem: 1–5 μm	Hem: < 1 μm; Cc: < 1 μm	< 0.5 μm
Internal texture	Spherules, aggregates, tubes- and stalk-like	Aggregates, spherules	Matrix, veins, crack fillings	Aggregates, spherules	Aggregates, spherules	Aggregates	Aggregates
Further characteristics	Chalcedony relics, syneresis cracks	Varying porosities, syneresis cracks	Pores within and along grains	Nanocrystalline sd replacing hematite	Sponge spicule	Only relics present	Replacement as veins, along grain boundaries or pervasively
Domain occurrence in ores							
Sedimentary-type quartz-haematite	+	+	+	-	-	-	-
Sedimentary-type siderite-haematite	-	±	±	+	±	-	-
Replacement-type calcite-haematite	-	-	-	-	-	±	+

Sedimentary-type siderite-haematite ores

Several ores display a more diverse mineralogy consisting of siderite and haematite, together with varying amounts of magnetite and quartz (Fig. 4a, b). The microdomains of these ores have been identified as siderite-haematite, siderite-magnetite-haematite, haematite, and quartz microdomains (Table 1).

The siderite-haematite microdomain is characterised by tabular haematite (< 500 nm) finely dispersed within single siderite crystals (0.1–2 mm; Fig. 4c). Locally, nanocrystalline siderite replaced haematite crystals (Fig. 4d). This microdomain forms aggregates in which haematite is either homogeneously or heterogeneously distributed (Fig. 4c). Rarely, haematite-rich spherules occur within a siderite matrix (Fig. 4e). Siderite-magnetite-haematite microdomains are mineralogically more complex and comprise granular subhedral magnetite (1–5 μm) and haematite (1–5 μm) homogeneously distributed in siderite (Fig. 4f). Texturally, the microdomains form aggregates and spherules. In the aggregates, magnetite and haematite are typically homogeneously distributed, whereas in the spherules (20–50 μm; Fig. 4f), these minerals form clusters characterised by a siderite-rich core and a magnetite-haematite-rich rim rarely surrounded by crescent-shaped cracks. Haematite and quartz microdomains in siderite-haematite ores commonly show similar features compared to equivalent microdomains in the haematite-quartz ores. If present, the haematite microdomains occur solely as aggregates.

Replacement-type calcite-haematite ores

Metasomatic replacement in ores of the Briloner Eisenberg mine is mainly characterised by veins that cut limestone along calcite grain boundaries or locally by pervasive replacement of limestone (Fig. 5a). Replacement textures are heterogeneously distributed, leading to variable ore grades. The replacement-type ore contains only haematite. In the replacement haematite microdomain, haematite occurs as aggregates of submicron-scale sub- to euhedral crystals less than 0.5 μm in size (Fig. 5b; Table 1).

Additionally, relics of calcite-haematite microdomains have been observed. This microdomain consists of haematite (< 1 μm) heterogeneously dispersed in a matrix of micro-crystalline calcite (Fig. 5c; Table 1), in which haematite crystals cut calcite grain boundaries. This microdomain is largely overprinted by replacement haematite microdomains and consequently only relics remain.

Volcaniclastic and clastic components in iron ores

Several samples collected in the Fortuna mine show variable amounts of volcaniclastic and clastic components. These ores occur in position A ore lenses, where footwall and hanging wall volcaniclastic rocks are mixed with ores (Fig. 6a), also at the footwall and hanging wall contacts of, and in the middle (one sample), of the position B ore (Fig. 6b). Incorporated volcaniclastic material ranges in size from ash to lapilli, whereas clastic material is fine-grained (Fig. 6c). These ores comprise features that are typical of sedimentary-type ores including haematite and lesser quartz-haematite and quartz microdomains; they, however, also display haematite replacement textures in volcaniclastic and clastic material (Fig. 6c, d). Volcaniclastic and clastic components have not been observed in the ores of the Briloner Eisenberg mine.

Fig. 5 Petrographic images of replacement-type calcite-haematite ores from the Briloner Eisenberg mine. **a** Photomicrograph of sample DSEb005 (position B) mainly consisting of replacement haematite microdomains. **b** Replacement of limestone along calcite grain boundaries by haematite replacement microdomain. **c** Micritic calcite with dispersed nanocrystalline haematite forming calcite-haematite microdomains. **b**, **c** reflected light photomicrographs. hem, replacement haematite microdomain; cc-hem, calcite-haematite microdomains (cc, calcite; hem, haematite; qz, quartz)
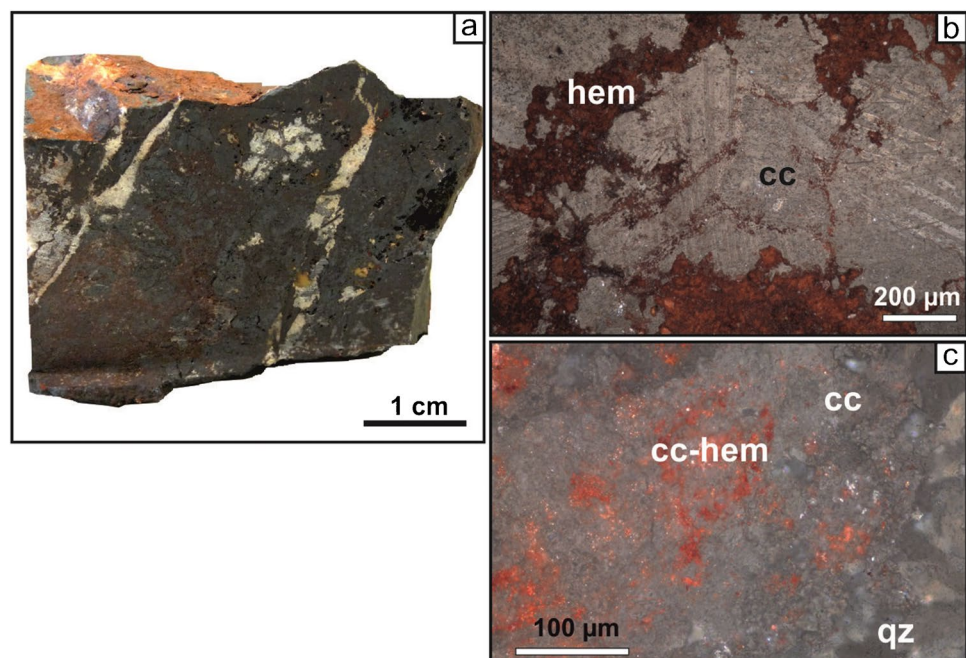
Fig. 6 (Volcani)clastic contamination and hydrothermal alteration in Fortuna and Briloner Eisenberg mine ores. **a** Haematite-quartz ore (Fortuna mine position A; DLFo014) mixed with footwall and hanging wall rocks. **b** Volcaniclastic contamination of haematite-quartz ore in the Fortuna mine. Volcaniclastic textures are preserved (position B; DLFo031). **c** Haematite microdomain partially replacing fine-grained hanging wall clastic sedimentary material. **d** Haematite microdomain filled gas pore in volcaniclastic components within the Fortuna mine. **e** Haematite-chlorite-quartz alteration overprinting haematite microdomains in the Fortuna mine. **f** Quartz alteration overprinting replacement-type calcite-haematite ores in the Briloner Eisenberg mine. **c–e** Reflected light photomicrographs, **f** transmitted light photomicrograph. For mineral abbreviations, see the caption of Fig. 5
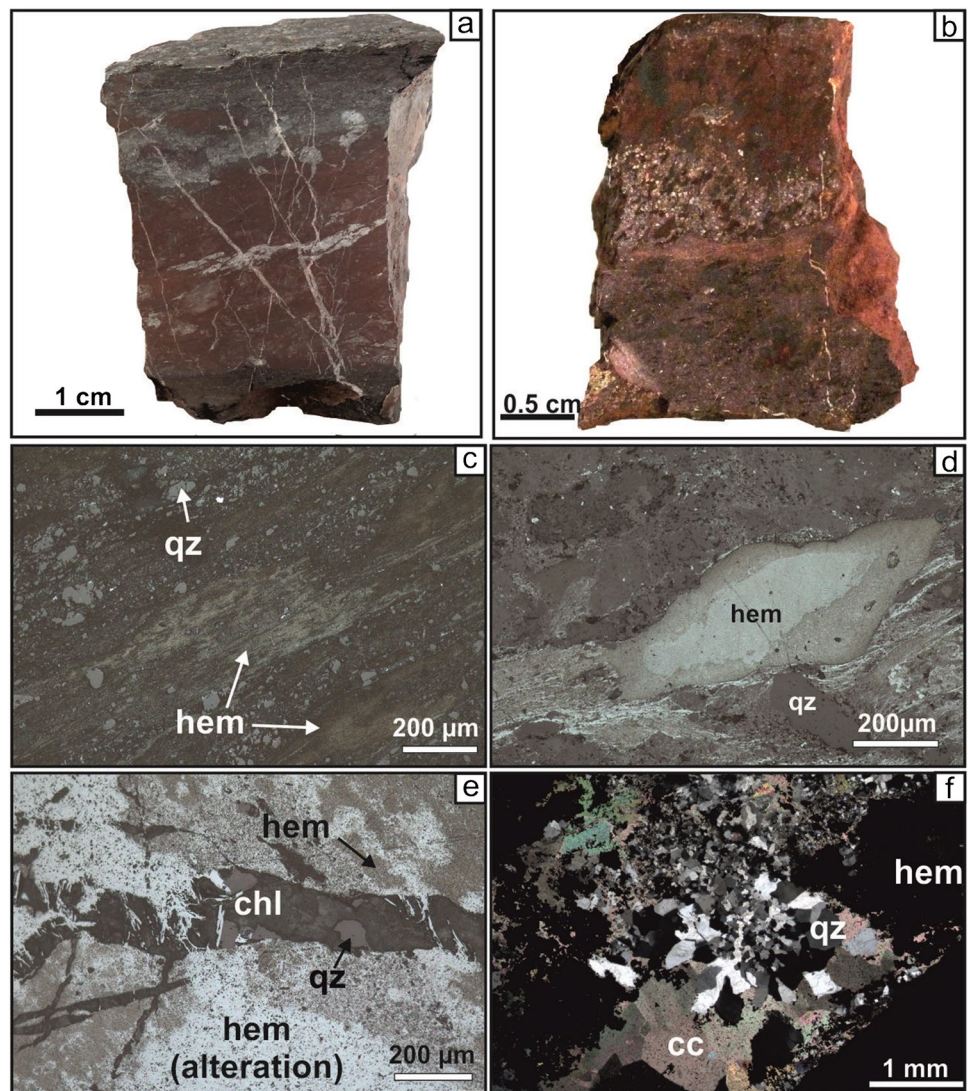
Hydrothermal alteration in iron ores

Several stages of hydrothermal veins cut the ores within the Fortuna mine. All these veins comprise varying amounts of quartz, carbonates (siderite, ankerite, calcite), chlorite, haematite, apatite, and minor pyrite and chalcopyrite (Fig. 6e). Haematite related to hydrothermal alteration is distinctly different compared to haematite associated with ore microdomains. The alteration-related haematite forms large euhedral crystals of up to 200 μm in size (white in reflected light), cross-cuts microdomains as veins, or forms schlieren within quartz-haematite and haematite microdomains (Fig. 6e). In two Fortuna mine ore samples (DLFo009, DLFo029), hydrothermal alteration is recorded by strong enrichment of secondary haematite in which the haematite forms large euhedral crystals that overgrew haematite microdomains or as replacements of them. Hydrothermal apatite forms veins and large single crystals (5–20 μm). A post-depositional overprint in the siderite-haematite ores is also defined by siderite-haematite microdomain aggregates that show evidence of siderite remobilisation leading to patchy haematite distribution and porous siderite rims (Fig. 4c). Hydrothermal alteration within the Briloner Eisenberg mine ores is characterised by veins cross-cutting the replacement- and sedimentary-type ores and host limestone. Veins comprise quartz, calcite, chlorite, haematite, and apatite with varying thicknesses from 5 to 500 μm. Quartz veins that cut the ores are abundant and reach up to 200 μm in thickness (Fig. 6f).

Footwall volcaniclastic rocks

Primary minerals in the footwall volcaniclastic rocks are plagioclase, clinopyroxene, olivine, amphibole, biotite, apatite, titanomagnetite, ilmenite, and volcanic glass (Nesbor et al. 1993), but they have been altered by seawater-rock interaction (seafloor alteration) and Variscan overprints (Nesbor 2004). Secondary minerals include albite, chlorite (mainly

chamosite), calcite, quartz, phengitic white mica, sericite, leucoxene, and minor ankerite, apatite, and haematite (Fig. 7). Albite phenocrysts are more prominent in green compared to purple volcaniclastic rocks and are commonly replaced in both by chamosite, calcite, and sericite (Fig. 7c). Primary volcanic glass is scarcely visible and mainly replaced by chamosite, calcite, quartz, phengitic white mica, and leucoxene with minor ankerite and apatite. Calcite typically forms several generations of cement, with grain sizes of up to 4 mm, and is the predominant phase in both green and purple volcaniclastic rocks (40–43 vol.%,) as determined by optical methods (SM3 in the online supplementary material). Note that geochemical analyses indicate a slightly higher calcite cement content in the purple volcaniclastic samples. Vesicles occur ubiquitously throughout the entire volcaniclastic sequence and are mainly filled by calcite, with minor chamosite, phengitic white mica, and quartz. In the purple volcaniclastic rocks, haematite is a minor phase (~8 vol.%; SM3 in the online supplementary

material) that replaces leucoxene as well as chamosite-filled vesicles; haematite also occurs along albite and calcite grain boundaries (Fig. 7d, e). Notably, the uppermost sample (DLFo016R) from 0.4 m beneath the position B ore layer shows a different mineralogy. The purple and strongly schistosed rock there mainly consist of phengitic white mica, chamosite and leucoxene, whereas calcite and albite phenocrysts are absent (Fig, 7 e, f). In addition, fine-grained quartz and haematite form abundant lenses up to 1.5 mm long and ca. 30 μm thick parallel to schistosity (Fig. 7f).

Whole-rock geochemistry of footwall volcaniclastic rocks

Footwall volcaniclastic rocks within the Fortuna mine have alkali to sub-alkali basaltic compositions (Fig. 8). Although these compositions are broadly similar, the

Fig. 7 Footwall volcaniclastic rocks from the Fortuna mine. **a** Green and **b** purple footwall volcaniclastic rocks. **c** Transmitted light photomicrograph showing mineral assemblage within green and **d** within purple volcaniclastic rocks. **e, f** Uppermost purple volcaniclastic rock sample (DLFo016R) with **e** haematite replacing chlorite in former gas pores and leucoxene and **f** quartz-haematite lenses parallel to schistosity. ab, albite; ank, ankerite; cc, calcite; chl, chlorite; hem, haematite; lcx, leucoxene; phg, phengitic white mica; qz, quartz
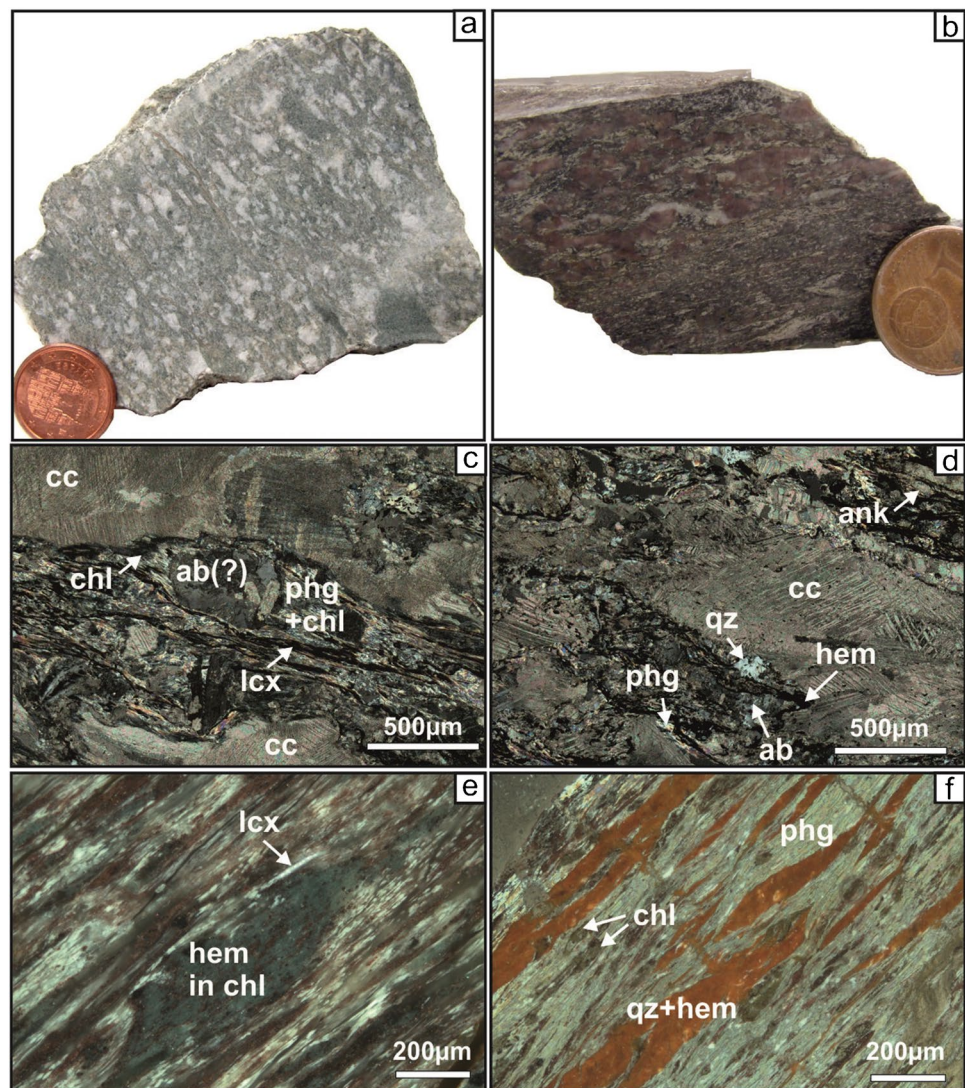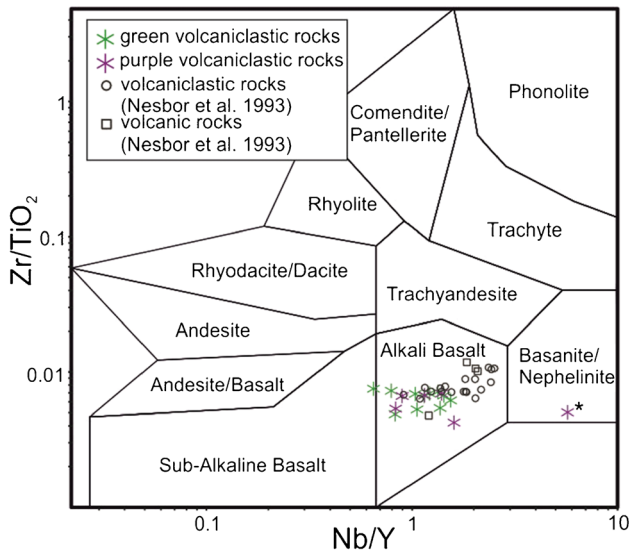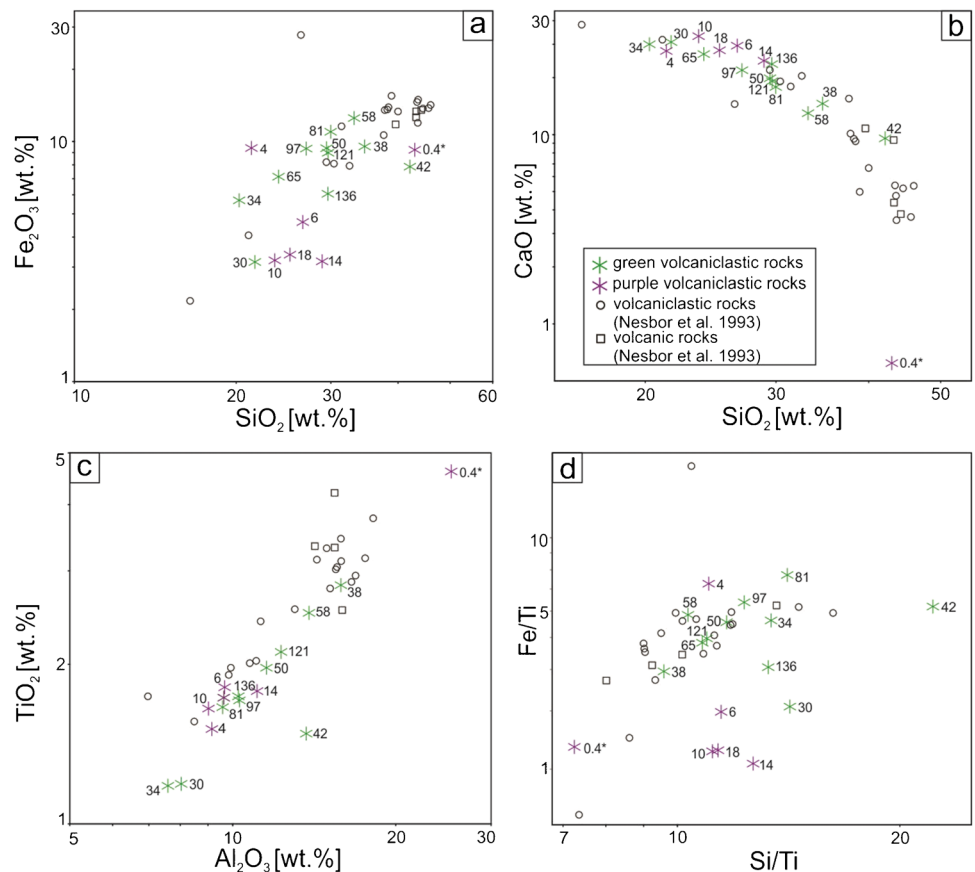
Fig. 8 Nb/Y vs. Zr/TiO$_2$ plot (after Winchester and Floyd 1977) depicting alkali basaltic character of Fortuna mine footwall and other local volcanic and volcaniclastic rock. Atypical sample DLFo016R is marked with a star

large variation in major element contents including SiO$_2$ (21–43 wt%), CaO (0.5–33 wt%), and Fe$_2$O$_3$ expressing total iron (Fe$_2$O$_3$; 3–13 wt%) is in contrast to most

regional Middle/Upper Devonian alkali basaltic rocks in the Lahn and Dill synclines (Fig. 9; Nesbor et al. 1993; Nesbor 2004). A negative correlation between SiO$_2$ and CaO is evident among all samples, with the purple volcaniclastic rocks being enriched in CaO and depleted in SiO$_2$ (Fig. 9b). Fe$_2$O$_3$ averages 6 wt% in the purple varieties compared to 8 wt% in the green varieties. A sharp decrease of Fe$_2$O$_3$ and SiO$_2$ occurs between 35 and 10 m below the ore boundary that corresponds to the transition from green to purple volcaniclastic rocks. Fe$_2$O$_3$ and SiO$_2$ increase again towards the ore body, whereas CaO contents display a different trend (Fig. 10). Contents of TiO$_2$ and Al$_2$O$_3$ are essentially uniform throughout the sequence (Fig. 9c). The purple volcaniclastic rocks have lower Fe/Ti and comparable Si/Ti ratios to the green volcaniclastic rocks and to those of other volcanic and volcaniclastic rocks in the Lahn and Dill synclines (Fig. 9d). The only exception is sample DLFo016R (0.4 m), which is characterised by higher TiO$_2$, Al$_2$O$_3$, and Nb/Y ratios (Figs. 8 and 9c). High SiO$_2$ and Fe$_2$O$_3$, and low CaO contents reflect the absence of calcite and increased content of phengitic white mica, chamosite, and quartz-haematite lenses in this sample (Fig. 9a, b).

Fig. 9 Major element plots of Fortuna mine footwall and other local volcanic and volcaniclastic rocks. SiO$_2$ vs. **a** Fe$_2$O$_3$ and **b** vs. CaO. **c** Al$_2$O$_3$ vs. TiO$_2$ and (**d**) Si/Ti vs. Fe/Ti diagrams. Numbers indicate the volcaniclastic footwall sample distance to position B ore contact in metres. Atypical sample DLFo016R is marked with a star

Fig. 10 Downhole plots of footwall volcaniclastic rocks of the Fortuna mine of **a** Fe_2O_3, **b** SiO_2, and **c** CaO. Zero indicates contact to position B ore. Bars in lower part of the plots indicate compositional ranges of other regional Middle/Upper Devonian volcanic and volcaniclastic rocks (Nesbor et al. 1993) and circles in bars indicate medians
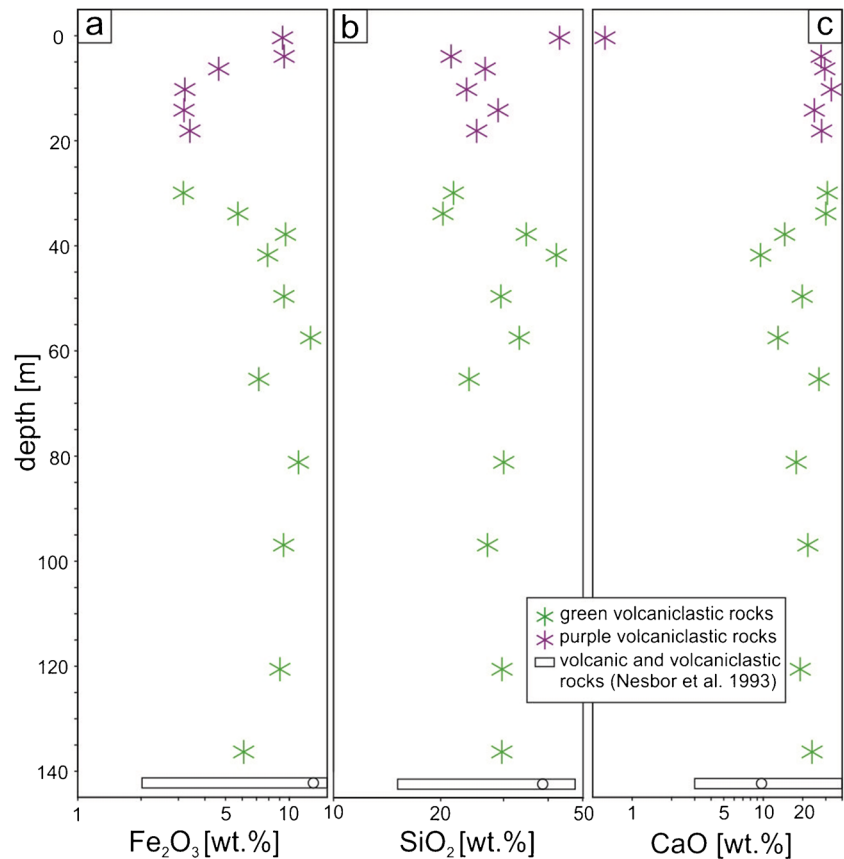
Discussion

Fe and Si sources

Mobilisation of Fe from volcaniclastic rocks is evident from footwall strata in the Fortuna mine that are depleted in Fe (avg. of 5 wt%) relative to regional volcanic and volcaniclastic rocks in the Lahn and Dill synclines that typically contain 9 wt% Fe on average (SM2 in the online supplementary material). Mass-balance calculations by Hentschel (1960) showed that 1 wt% Fe loss in a 250-m-thick volcaniclastic sequence is sufficient to form a 4-m-thick ore layer averaging 40 wt% Fe. Taking average Fe values (40 wt%) from Schmitt et al. (n.d), mass-balance calculations for the Fortuna mine (SM4 in the online supplementary material) suggest that a loss of 2 wt% Fe in a 136-m-thick sequence of volcaniclastic rocks would be needed to form the position B ore body. Similar calculations for Si (avg. 15 wt%; Schmitt et al. n.d), volcaniclastic rocks would have lost 1 wt% Si to form an ore averaging 15 wt% Si. Release of Fe during alteration of the volcaniclastic rocks is consistent with evidence of basalts that show a high Fe mobilisation potential during sea-water alteration (Stranghoener et al. 2020). Therefore, using this model, we suggest that a sequence of 136 m of volcaniclastic rocks would have provided sufficient Fe and Si to form the Fortuna mine iron ores.

Processes of iron mobilisation

Mobilisation of Fe in volcaniclastic rocks, as suggested in the previous section, is likely related to extensive low-temperature hydrothermal alteration by seawater (cf. Schmitt et al. n.d). Such alteration of volcaniclastic rocks is preserved in the entire 136 m sequence and evident from the presence of albitised rocks, abundant carbonate-filled vesicles and replacement of the (scarcely preserved) primary glass matrix by chlorite, phengitic white mica, calcite and quartz (Fig. 7c, d). Albitisation and carbonate formation could have taken place via uptake of CO_2 resulting in H_2CO_3-rich fluids. CO_2 may have been provided by eruptive and/or diffuse volcanic degassing which is well known from several modern volcanic systems (e.g., Aubaud et al. 2005; Melián et al. 2014). Additionally, CO_2 may be derived from seawater circulation (Nakamura and Kato 2004) through volcaniclastic rocks and porosity-trapped seawater during the deposition of volcaniclastic rocks. In this model, the alteration of primary olivine, pyroxene and plagioclase by H_2CO_3-rich fluids caused a release of cations (e.g., Mg, Ca, Fe, Si) that become available for additional calcite, chlorite, and phengite formation (e.g., Gudbrandsson et al. 2011; Luhmann et al. 2017). Ascending fluids resulting from the described alteration of volcaniclastic rocks are interpreted

to be reduced and near-neutral to slightly alkaline. Low Eh is likely evident from the mobilisation of Fe^{2+} from the volcaniclastic rocks as well as from modern hydrothermal vent fluids being commonly reduced (German and Seyfried 2014 and references therein), and fluids are likely near-neutral to slightly alkaline due to volcaniclastic rocks losing the capacity to buffer fluids to a lower pH with protracted water–rock interaction (Flaathen et al. 2009; German and Seyfried 2014; Luhmann et al. 2017). The absence of sulfides and sulfide fronts within the footwall volcaniclastic rock, as well as the lack of sulfide concentrations associated with the Lahn-Dill-type iron ores suggest that the involved fluids were H_2S-poor.

The volcaniclastic rocks in the study area are commonly green owing to chlorite formation during the above-described water–rock interactions. The upper 18 m of the volcaniclastic sequence, however, show a purple colour related to the presence of haematite. The haematite replacement of secondary minerals including a leucoxene phase and chamosite may be explained by extended interaction with oxygenated seawater, leading to superimposed alteration subsequent to the earlier seafloor alteration. Formation of haematite during protracted seawater-rock interaction is described, for instance, from the hydrothermal alteration of oceanic crust (Alt et al. 2010), from the seafloor alteration of volcanic facies (Dimroth and Lichtblau 1979; Gifkins and Allen 2001; Kruber et al. 2008), and is supported by experiments (Seyfried and Mottl 1982).

The uppermost 4 m of the volcaniclastic sequence (represented by samples DLFo016R and DLFo017R; Fig. 10a) has much higher Fe_2O_3 compared to other purple volcaniclastic rocks. Sample DLFo016R also contains quartz-haematite lenses (Fig. 7f). This geochemical and petrographic anomaly directly below the position B ore may be explained by descending infiltration of mobile, Fe-Si-rich gels from the primary ore superseding the less dense pore-water in volcaniclastic sediments, an interpretation similar to that of Rösler (1962), who described similar textures in Lahn-Dill-type iron ores in the Bergaer anticline, and a scenario similar to the massive sulfide mud infiltration model of Sangster (2001). Alternatively, semi-consolidated Fe-Si-rich gel may also have mixed with the semi-consolidated underlying volcaniclastic material, which may have led to textures seen in position A ores (Fig. 6a).

Fe-(oxyhydro)oxide precipitation and sedimentation

Quartz-haematite, haematite, and quartz microdomains are the product of the dominant sedimentary ore-forming process that formed the iron ores of the Fortuna mine. Calcite-haematite microdomains likely preserve primary textures recording depositional processes within the Briloner Eisenberg mine. Textures, especially those present in the

haematite-quartz ores, reflect abiotic and biotic oxidation of ferrous Fe in a seawater column that likely was oxygenated.

Haematite dispersed in quartz (e.g., quartz-haematite microdomain aggregates) and in microcrystalline calcite (calcite-haematite microdomains) may be the diagenetic product of colloidal ferrihydrite (general formula $Fe_5O_8H \cdot H_2O$; Cornell and Schwertmann 2003) that formed in an oxygenated seawater environment (Fig. 10a). This model is consistent with the Rhenohercynian Basin having been fairly shallow (< 200 m; Nesbor 2004), iron ore deposits being small and only occurring locally, as well as with a diverse macro and micro fauna being present locally (Harbort 1903; Bottke 1965; House and Ziegler 1977) due to ore formation on volcanic flanks close to the (inactive) volcanic centre (Bottke 1965). It furthermore is supported by Middle Devonian oceans being considered widely oxygenated (Elrick et al. 2022) and with colloidal Fe-(oxyhydr)oxides as the predominant Fe mineral phase in (modern) oxygenated oceans (Bergquist et al. 2007). The microdomains in Fortuna mine ores show ocean island basalt-normalised REY patterns that are characterised by negative (apatite-controlled trace element patterns) or by absence of Ce anomalies (haematite-controlled trace element patterns), both being indicative of formation in an oxidised environment (Schmitt et al. n.d, and references therein). Therefore, in the case of the haematite-quartz ores, ferrihydrite may have scavenged silica in the oxidised water column (Grenne and Slack 2003b). It has been shown in experiments (Davis et al. 2002) and natural systems (Bergquist et al. 2007) that silica is readily adsorbed onto Fe-(oxyhydr)oxide particles. Experiments also show that ferrihydrite that forms abiotically via several intermediate products is a common precursor to haematite in aquatic systems (Schwertmann et al. 1999). We therefore infer that in Lahn-Dill-type iron ores, ferrihydrite was a precursor that formed in a dominantly oxygenated environment.

However, oxidation of Fe^{2+} may also have locally occurred in an environment characterised by partial suboxic conditions. The presence of tube and filamentous stalk-like textures (Fig. 3j) within the haematite-quartz ores implies involvement of biotic Fe oxidation. These tube and filamentous stalk-like textures may have formed inorganically ("chemical gardens") sensu McMahon (2019). More likely, however, they are primary textures related to biotic Fe oxidation. Observed twisted, branching, and coordinated growth features (Fig. 3j) resemble the textures seen in microbial mats living at modern low-temperature vent sites (Scholten et al. 2004; Edwards et al. 2011; Chan et al. 2016; Esposito et al. 2018; González et al. 2020). These microbial communities commonly form proximal to vent sites at the interface between oxygenated seawater and reduced hydrothermal fluid (Little et al. 2021). Tube and filamentous stalk-like textures may therefore be regarded as

primary features indicative of vent proximity and recording Fe-oxidising bacterial activity within the Lahn-Dill-type iron ore system.

Haematite-quartz ore formation

Mineralogical and textural features down to the nanometre-scale in the quartz-haematite microdomains are interpreted as products of primary deposition and early diagenesis. Quartz-haematite microdomain spherules are considered primary textures and are known to form by inorganic

consolidation and dehydration of Fe-Si-rich gels (Gránásy et al. 2005). Similar inorganic spherules have been described from marine Fe-oxide occurrences of varying ages and settings (Duhig et al. 1992; Grenne and Slack 2003a; Jorge et al. 2005). Aggregates formed by quartz-haematite and haematite microdomains are interpreted as primary and early diagenetic textures that may have formed by two different processes: fluctuating vent activity and diagenetic gel maturation (Fig. 11). Fluctuating vent activity in the Lahn-Dill-type iron ore vent system implies varying fluid flow rates and Fe concentrations. Transient
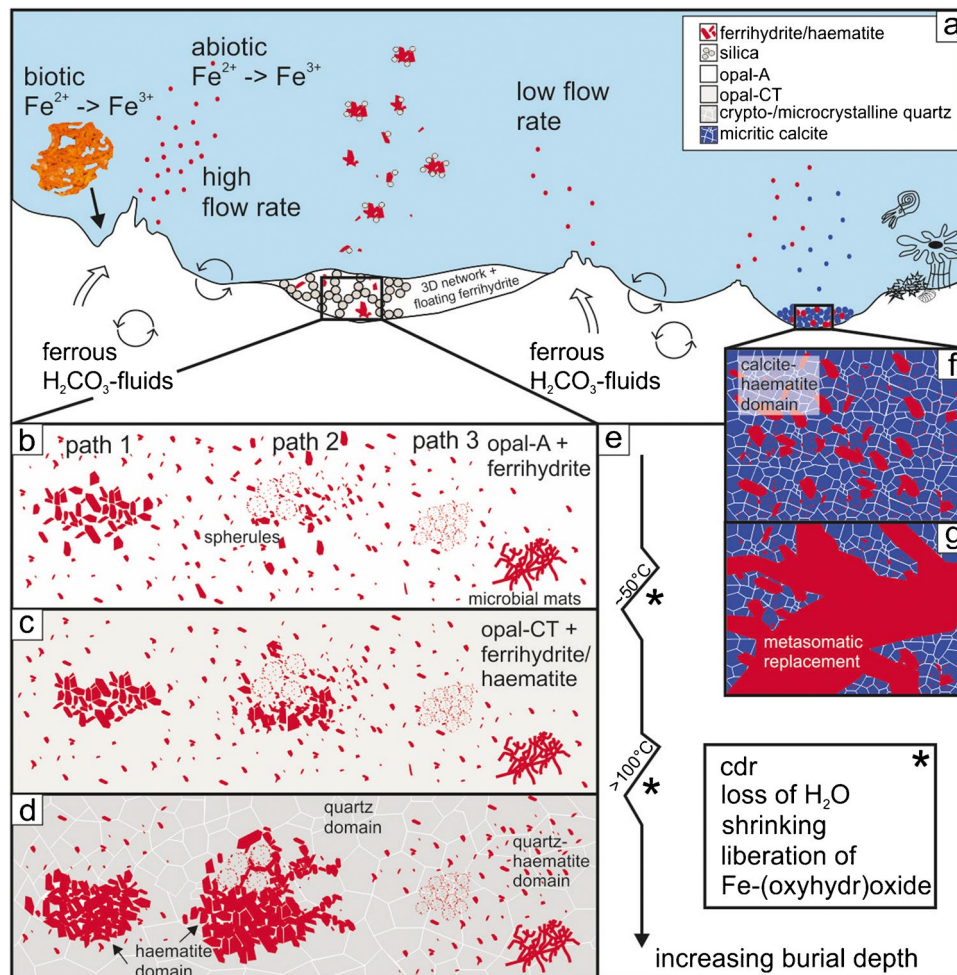
Fig. 11 Genetic model of Lahn-Dill-type iron ore formation. **a** Fe mobilisation by H_2CO_3-fluids that vent into the ocean, with Fe^{2+} oxidised biotically and abiotically to Fe^{3+}. Scavenging of silica onto ferrihydrite leads to gel formation (sedimentary-type haematite-quartz ores) or contemporaneous sedimentation of ferrihydrite with carbonates leads to formation of Fe-rich carbonate mud (replacement-type calcite-haematite ores). **b–d** Possible formation pathways of quartz-haematite, haematite, and quartz microdomains in sedimentary-type haematite-quartz ores related to varying fluid flux, gel formation, and diagenetic maturation. Path 1 depicts haematite microdomain formation related to high fluid flux. Increased burial depth leads to accumulation of ferrihydrite/haematite and incomplete separation of quartz

from haematite resulting in quartz-haematite microdomains. Path 2 shows haematite and quartz microdomain formation during periods of low fluid flux. Note accumulation of haematite along quartz grain boundaries related to separation of quartz from haematite. Path 3 displays quartz-haematite microdomain formation due to incomplete separation of haematite from quartz. **e** Processes associated with transitions from opal-A to opal-CT and quartz, respectively, during diagenetic gel maturation. cdr, coupled-dissolution-reprecipitation. **f** Formation of replacement-type calcite-haematite ores related to coprecipitation of ferrihydrite with carbonate mud and **g** subsequent metasomatic replacement by haematite

high flow rates and abundant colloidal ferrihydrite lead to the formation of both haematite- and quartz-haematite microdomains (path 1 in Fig. 11b–d). During these high flow rates, silica is readily adsorbed onto ferrihydrite, resulting in quartz-haematite microdomains. Uptake of silica onto ferrihydrite inevitably causes zones of silica depletion within the water column (Sherrell et al. 1999). Ferrihydrite sinking through such zones of silica depletion can form haematite microdomains. Low flow rates and formation of particulate Fe-(oxyhydro)oxides tend to promote the formation of quartz-haematite microdomains related to the absence of local zones of silica depletion (paths 2 and 3 in Fig. 11b–d). Temporal changes including flow rates are a common feature in modern seafloor-hydrothermal vent systems (von Damm 1995; German and Seyfried 2014) and as suggested here also within the vent systems attributed to the formation of Lahn-Dill-type iron ores.

Additionally, in our model quartz-haematite, haematite and quartz microdomains segregated during early diagenetic gel maturation. Early diagenetic textures include, for example, typical halos of quartz-haematite microdomains surrounding cores of haematite microdomains (Fig. 3i), and haematite crystal cumulates within pores in quartz grains and along quartz grain boundaries (Fig. 3c–g). Abundant uptake of silica onto ferrihydrite causes polymerisation and coagulation into a network, forming a silica gel with ferrihydrite particles "floating" within (Iler 1979) — the starting phase to form quartz-haematite, haematite, and quartz microdomains during early diagenetic gel maturation (paths 2 and 3 in Fig. 11b–d). The spatial association of haematite with quartz pores at the interface of haematite to quartz-haematite microdomains (Fig. 3f) is explained by the liberation of ferrihydrite particles during amorphous silica transformations and subsequent accumulation of precursor ferrihydrite in pore space during diagenetic gel maturation. In aquatic systems at high salinity, the transformation of silica gel to opal-A and then to opal-CT occurs at temperatures of ca. 50 °C and subsequent transformation to crypto- and microcrystalline quartz at temperatures of > 100 °C (Murata and Larson 1975; Kastner et al. 1977). These mineral transformations are accompanied by dehydration, shrinking, and pore formation (Fig. 11e) related to dissolution and re-precipitation of the silica (cf. Williams and Crerar 1985). The resulting ferrihydrite and opal-dominated microdomains are precursors to the haematite and quartz microdomains, respectively. Where separation was incomplete, opal-ferrihydrite microdomains remain, thus providing the precursor for the quartz-haematite microdomains (path 3 in Fig. 10b–d). The ferrihydrite to haematite transformation is likely triggered during early diagenesis related to the accumulation of Fe-(oxyhydr) oxide particles facilitating crystallisation to haematite (Schwertmann et al. 1999).

Siderite-haematite ore formation

Within the Fortuna mine, the position B ore body shows an increased abundance of siderite-haematite and siderite-magnetite-haematite microdomains at the top. The change in mineralogical composition from stratigraphically lower quartz-haematite-rich microdomains to siderite-haematite-rich microdomains may reflect a change of physico-chemical parameters in the basin at the place of ore formation or post-depositional Fe reduction. Primary deposition of siderite in equilibrium with haematite and/or magnetite may be possible at near-neutral pH, and under suboxic conditions (Huber and Garrels 1953). Figure 4d shows nanocrystalline siderite replacing euhedral haematite crystals, which was likely followed by annealing and crystal growth to larger siderite crystals, including the existing euhedral haematite, thus as a result forming the siderite-haematite microdomains. This conclusion is supported by the observation that the haematite inclusions in siderite are randomly oriented with respect to siderite, implying a post-depositional formation of the siderite-haematite microdomains. Therefore, siderite likely formed either via abiotic or biotic iron reduction during diagenesis (Heimann et al. 2010; Köhler et al. 2013) or by reduction of Fe during metamorphism (Halama et al. 2016). Iron reduction can alternatively lead to the formation of siderite, magnetite, and haematite (siderite-magnetite-haematite microdomains), as shown experimentally by Köhler et al. (2013). The formation of siderite requires carbon, which could have been provided by local volcanic degassing of CO_2, or by input of organic carbon, though the nearest reefs are ca. 2.5 km off the Fortuna deposit (cf. Figure 1b), and therefore representing an unlikely carbon source.

Post-mineralisation processes

The haematite-quartz ores contain relics of biogenic textures (Fig. 3j) and chalcedony (Fig. 3k) that are widely considered as fragile constructs prone to destruction by metamorphism (Little et al. 2021). Preservation of such features demonstrates that deformational and metamorphic overprints of the ores were minimal. However, several textures in the microdomains of sedimentary-type haematite-quartz and siderite-haematite ores may reflect a metamorphic overprint: the presence of sharp contacts between microdomains related to grain-boundary re-equilibration during elevated temperatures (Vernon 1976; Kruhl and Peternell 2002), as well as the occurrence of intergranular pores in haematite microdomains and pores along quartz boundaries in the quartz-haematite and quartz microdomains. Similar pores are known to occur in regionally metamorphosed rocks at low to medium grade and are attributed to crystal size reduction and partial dissolution during cooling after peak

metamorphism (Kruhl et al. 2013). Siderite-haematite and siderite-magnetite-haematite microdomains display haematite-free rims with high porosity as well as patchy distributions of haematite and magnetite (Fig. 4c, f). Porous rims are typically related to hydrothermal alteration and associated processes of coupled-dissolution-reprecipitation (Putnis 2002). Low-grade metamorphism led to grain growth of quartz, haematite, siderite, and magnetite and weak ductile deformation that produced subgrain formation in quartz (Fig. 3e).

Replacement-type ores

The ores within the Briloner Eisenberg mine formed by a two-step process: chemical sedimentation of calcite and ferrihydrite and subsequent metasomatic replacement. Rare textures of nanocrystalline haematite finely dispersed within microcrystalline calcite (calcite-haematite microdomain; Fig. 5c) indicate precipitation of ferrihydrite and calcite from $CaCO_3$-saturated seawater. This interpretation is supported by evidence of contemporaneous massive reef formation (Briloner reef) in the vicinity of the Briloner Eisenberg deposit (Paeckelmann 1936; May 1987). Similar coprecipitation processes of calcite and Fe-rich particles have been described for several Lahn-Dill-type iron ore occurrences in the Harz Mountains in Germany (Harbort 1903), from the Carboniferous Tynagh iron formation in Ireland (Schultz 1966), and from other Phanerozoic limestone occurrences (Cruise 2000 and references therein).

Where calcite-haematite microdomains formed, limestone is metasomatically replaced by haematite along grain boundaries, pervasively or within veins (Fig. 5b). Haematised fossils have been found in the Harz Mountains related to Lahn-Dill-type iron ores (Harbort 1903) indicating that metasomatic replacement processes did not only occur in the East Sauerland anticline. Despite metasomatic processes that must have taken place after consolidation of a ferrihydrite-carbonate mud, these processes are also related to the Lahn-Dill-type iron ore system. This interpretation is supported by the presence of sedimentary-type haematite-quartz ores on top of the metasomatically replaced limestone.

The Lahn-Dill-type iron ore system — from regional to global perspectives

Devonian Lahn-Dill-type iron ores *sensu stricto* occur within the eastern Rhenish Massif, the Harz Mountains, the central Saxothuringian Zone, and the eastern Sudetes (Fig. 1a; Table 2). The ores are intimately linked to mafic volcanic and volcaniclastic rocks; are confined to local strata that were deposited in restricted, shallow marine basins in the Rheic Ocean (Fig. 12); and are mineralogically dominated by haematite and quartz. Formation of the iron ores was related to chemical precipitation in a largely oxidised environment and subordinately to metasomatic replacement of wall rocks. No stratigraphic and temporal association exist with other types of deposits (e.g. base metals, Mn). Owing to these distinctive characteristics, the Lahn-Dill-type iron ores have usually been considered a rather unique deposit type (Quade 1968; Bottke 1981). However, several similar marine volcanic-associated Fe-oxide occurrences are known in the eastern Alps (e.g. Gurktal Nappe, Heugraben, Plankogel, Jochberg, Sausal), western Carpathians (Vaporicum, Gemericum), southern Carpathians (Poiana Ruscă Mountains), Dinarides (Medvenica and Ključ), and the Iberian Pyrite Belt (Table 2). All of these occurrences are limited to Silurian to Carboniferous (semi-)restricted shallow marine basins and are linked to mafic, or to subordinately intermediate to felsic volcanic and volcaniclastic rocks (cf. Table 2), and hence are potential Lahn-Dill-type iron ore equivalents. In the Iberian Pyrite Belt, some of the Fe-oxide occurrences are interpreted to have formed due to chemical sedimentation and metasomatic wall rock replacement (Leistel et al. 1997). All of them, including the Lahn-Dill-type iron ores, mainly display a massive texture compared to Precambrian and Early Palaeozoic occurrences that display cyclic layering and banding (Table 2). The massive texture in Lahn-Dill-type ores and other Silurian to Carboniferous occurrences is interpreted to be related to local formation on volcanic flanks (cf. Bottke 1965), a setting in which slumping of semi-consolidated sediments could lead to complex textures and absence of distinct layering. The dominance of haematite in those Fe-oxide occurrences may be suggestive of formation in largely oxidised basins.

Carboniferous Fe-oxide occurrences in the eastern Rhenish Massif and the Harz Mountains formed within sedimentary facies comparable to those of the Lahn-Dill-type iron ores. They are associated with tholeiitic basalt, display similar textures, and can be explained by similar formation processes (Schaeffer 1980; Felgentreu 2020). Most of them are characterised by high SiO_2 (> 90 wt%) and low Fe_2O_3 (4–6 wt%) contents (Lippert 1970). However, some occurrences contain Mn minerals (Huckriede 1996). Similarly, Carboniferous Fe-oxide occurrences in the Central Midlands Basin in Ireland (e.g. Tynagh, Crinkill, and Lisheen deposits) show evidence of strikingly similar formational processes including precipitation on the seafloor and wall rock replacement but are not associated with volcanic and volcaniclastic rocks (Schultz 1966; Cruise 2000). Therefore, despite these similarities, the Carboniferous occurrences in Germany and Ireland are not considered to belong to the Lahn-Dill-type *sensu stricto*.

Table 2 Comparison of Lahn-Dill-type iron ores with other marine volcanic-associated Fe-oxide deposits and occurrences through time

Type	Exemplary area	Age	Footwall rocks	Tectonic setting	Extent	Textures	References
Precambrian volcanic-associated Fe-oxide occurrences (Algoma-type iron formation)	Pilbara craton, Australia; Kaapvaal craton, South Africa	Eoarchean to Palaeoproterozoic	Felsic to mafic volcanic and volcaniclastic rocks	Restricted basins (?)	Regional	Banded	Bekker et al. (2010); Konhauser et al. (2017)
Early Palaeozoic volcanic-associated Fe-oxide occurrences/ deposits	Mt. Windsor volcanic belt, Australia	Cambrian to Ordovicium	Mafic (to felsic) volcanic and volcaniclastic rocks	Continental margins of the Iapetus ocean	Local	Commonly banded to locally massive	Duhig et al. (1992)
	Lokken ophiolithe, Norway						Grenne and Slack (2003a)
	New Brunswick and Newfoundland, Canada						Goodfellow (2007); Skulski et al. (2009)
	Tyrone igneous complex						Hollis et al. (2015)
Middle Palaeozoic volcanic-associated Fe-oxide deposits (Lahn-Dill-type iron ores)	E Rhenish Massif (Rhenohercynian Zone), Germany	Middle to Late Devonian	Mafic volcanic and volcaniclastic rocks	Pre-Variscan restricted shallow marine basins	Local	Massive	Lippert and Flick (1998)
	Harz Mountains (Rhenohercynian Zone), Germany						Hesemann (1927)
	Central Saxothuringia (Saxothuringian Zone) Germany						Rösler (1962)
	Eastern Sudetes (Moravo-Silesian Zone), Czech Republic						Kretschmer (1899)
Middle to late Palaeozoic volcanic-associated Fe-oxide deposits/ occurrences (potential Lahn-Dill-type equivalents)	S Carpathians, Romania	Silurian to Carboniferous	Mafic (to felsic) Volcanic and volcaniclastic rocks	Pre-Variscan restricted shallow marine basins	Local	Massive	Kräutner (1977)
	E Alps, Austria						Weber (1997)
	W Carpathians, Slovakia						Radvanec and Grecula (2016)
	Dinarides, Croatia and Bosnia						Palinkaš et al. (2008)
	Iberian Pyrite Belt, Spain and Portugal						Leistel et al. (1997)
Modern volcanic-associated Fe-oxide occurrences	5 km off Hawaii, USA	Modern	Mafic volcanic rocks		Local	Massive	Edwards et al. (2011)
	El Hierro, Canary Islands						González et al. (2020)

Fig. 12 Palaeogeography during Middle to Late Devonian at ca. 380 Ma. Stars mark locations of Lahn-Dill-type iron ores (1–4) and potential equivalents (5–9). Note that several occurrences are slightly older (Silurian) or younger (Carboniferous), and therefore, their locations are approximations. Palaeogeographic map from Deep Time Maps™ 2020
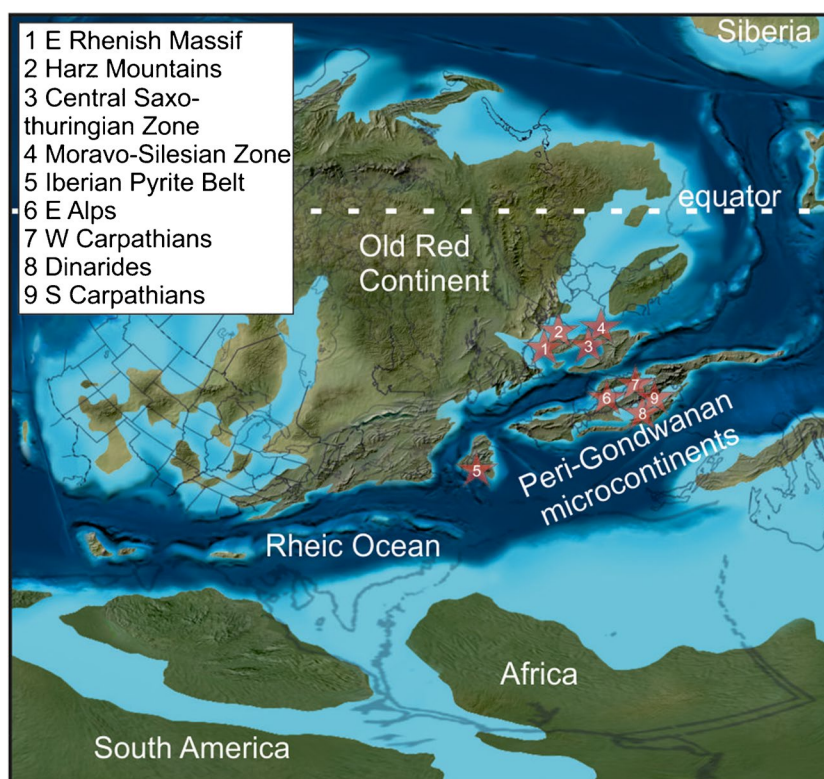
Older Fe-oxide occurrences have been described from numerous Precambrian basins, also referred to as the Algoma-type iron formations (Bekker et al. 2014 and references therein), as well as from Early Palaeozoic basins (Table 2). They share a link to volcanic activity and have many micro-textural characteristics like those of the Lahn-Dill-type iron ores suggesting comparable genetic processes. Similar micro-textures include the presence of haematite finely dispersed in quartz (Duhig et al. 1992; Grenne and Slack 2003a; Angerer et al. 2013; 2016; Egglseder et al. 2018; Abd El-Rahman et al. 2019), haematite associated with quartz pores (Egglseder et al. 2018), spherules surrounded by syneresis cracks (Duhig et al. 1992; Grenne and Slack 2003a), and tube and filamentous stalk-like textures (Duhig et al. 1992; Grenne and Slack 2003a; Dodd et al. 2017; Little et al. 2021; Papineau et al. 2022). However, they typically show an overall distinctive layered texture, have a basin-wide extent (Precambrian iron formations; cf. Table 2), and an association with base metal sulfide deposits (Early Palaeozoic occurrences; cf. Table 2).

Modern Fe-oxide accumulations that occur locally around Hawaii (Edwards et al. 2011) and El Hierro in the Canary Islands (González et al. 2020) are characterised by Fe-Si-rich gels that pool over volcanic rocks (Table 2). These occurrences may represent precursors to some of the micro-textures mentioned above, as well as being modern analogues to some of the Fe-oxide deposits and occurrences described herein.

Throughout Earth's history, largely comparable formation processes have been consistent and present a common link among many marine Fe-oxide deposits and occurrences. Such processes include the precipitation of Fe-rich particles coeval (or alternating) with amorphous silica and the formation of a Fe-Si-rich gel and its subsequent maturation (Duhig et al. 1992; Grenne and Slack 2003a; Edwards et al. 2011; Konhauser et al. 2017). Differences (texture, base metal- and Mn-mineral-association) may be explained by varying depositional environments by which, however, the formation of Lahn-Dill-type iron ores and equivalents seems to be limited to a time (Silurian to Carboniferous) during which restricted, shallow, and largely oxidised marine basins in the Rheic Ocean with extensive volcanic and hydrothermal activity prevailed (Fig. 12). In contrast, Precambrian Algoma-type iron formations and Early Palaeozoic Fe-oxide occurrences, for instance, formed in anoxic or stratified semi-restricted basins to open-marine settings (Konhauser et al. 2017; Grenne and Slack 2019). Therefore, the depositional environment, including, for instance, the location of deposition relative to the volcanic edifice, O_2 availability, absence or presence of seawater stratification and microbial activity, appear to be the crucial factors in determining the specific type of marine Fe-oxide deposits and occurrences.

Conclusions

State-of-the-art high-resolution petrography combined with whole-rock geochemical analysis of ores and footwall volcaniclastic rocks from two Lahn-Dill-type iron ore mines, Fortuna and Briloner Eisenberg, yielded new insights into marine haematite-rich ore formation from metal source to sink. The ore genesis is related to a complex interplay of hydrothermal, marine, microbial, diagenetic, and metasomatic processes, as follows:

- Ore formation was triggered by seawater trapped during the deposition of porous volcaniclastic rocks, subsequently mixing with volcanic-derived CO_2. Resulting H_2CO_3-rich and H_2S-poor fluids leached and mobilised Fe and altered footwall volcaniclastic rocks.
- Iron was mobilised from a subseafloor volcaniclastic sequence in a zone of at least 136-m-thickness. Mass-balance calculations show that this sequence contained sufficient Fe to serve as source for iron ore formation in the Fortuna mine.
- Ascending fluids either vented into marine basins forming sedimentary-type iron ores or metasomatically replaced wall rocks forming replacement-type iron ores.
- Haematite-quartz ores formed by Fe-Si-rich gel precipitation on the seafloor and subsequent maturation accompanied by mineral transformation of particulate ferrihydrite and silica-polymorphs (to haematite and quartz) and H_2O loss–related shrinking and liberation of ferrihydrite. Partial diagenetic Fe^{3+} reduction in haematite-quartz ores led to formation of the siderite-haematite ores.
- Chemical precipitation of calcite and ferrihydrite and subsequent metasomatic replacement led to calcite-haematite ore formation.

The formation of Lahn-Dill-type iron ores and their equivalents occurred during the Silurian to Carboniferous in restricted shallow marine basins within the Rheic Ocean. The interplay between extensive volcanism and hydrothermal flux in these likely oxygenated basins created a unique environment in which Lahn-Dill-type iron mineralisation was favoured.

Declarations

References

Abd El-Rahman Y, Gutzmer J, Li X-H, Seifert T, Li C-F, Ling X-X, Li J (2019) Not all Neoproterozoic iron formations are glaciogenic: Sturtian-aged non-Rapitan exhalative iron formations from the Arabian-Nubian Shield. Miner Deposita 55:577–596. https://doi.org/10.1007/s00126-019-00898-0

Ahlburg J (1911) Geologische Beziehungen zwischen den Eisenerzlagerstätten des Siegerlandes und des Lahn-Dillgebietes. Z Prakt Geol 1911:59–71

Alt JC, Laverne C, Coggon RM, Teagle DAH, Banerjee NR, Morgan S, Smith-Duque CE, Harris M, Galli L (2010) Subsurface structure of a submarine hydrothermal system in ocean crust formed at the East Pacific Rise, ODP/IODP Site 1256. Geochem Geophy Geosy 11:1–28. https://doi.org/10.1029/2010GC003144

Angerer T, Hagemann SG, Danyushevsky L (2013) High-grade iron ore at Windarling, Yilgarn Craton: a product of syn-orogenic deformation, hypogene hydrothermal alteration and supergene modification in an Archean BIF-basalt lithostratigraphy. Miner Deposita 48:697–728. https://doi.org/10.1007/s00126-012-0450-3

Angerer T, Hagemann SG, Walde DH, Halverson GP, Boyce AJ (2016) Multiple metal sources in the glaciomarine facies of the Neoproterozoic Jacadigo iron formation in the "Santa Cruz deposit", Corumbá, Brazil. Precambrian Res 275:369–393. https://doi.org/10.1016/j.precamres.2016.01.002

Aubaud C, Pineau F, Hékinian R, Javoy M (2005) Degassing of CO2 and H2O in submarine lavas from the Society hotspot. Earth Planet Sc Lett 235:511–527. https://doi.org/10.1016/j.epsl.2005.04.047

Bekker A, Slack JF, Planavsky N, Krapež B, Hofmann A, Konhauser KO, Rouxel OJ (2010) Iron formation: the sedimentary product of a complex interplay among mantle, tectonic, oceanic, and biospheric processes. Econ Geol 105:467–508. https://doi.org/10.2113/gsecongeo.105.3.467

Bekker A, Planavsky NJ, Krapež B, Rasmussen B, Hofmann A, Slack JF, Rouxel OJ, Konhauser KO (2014) Iron formations: their origins and implications for ancient seawater chemistry. In: MacKenzie FT (ed) Sediments, diagenesis, and sedimentary rocks. Treatise on Geochemistry, 2nd edn. Elsevier, Amsterdam, pp 561–628. https://doi.org/10.1016/B978-0-08-095975-7.00719-1

Bergquist BA, Wu J, Boyle EA (2007) Variability in oceanic dissolved iron is dominated by the colloidal fraction. Geochim Cosmochim Acta 71:2960–2974. https://doi.org/10.1016/j.gca.2007.03.013

Blakey RC (2020) © Deep Time Maps™ 2020, Paleozoic: 380 Ma Moll_Dev (URL: https://deeptimemaps.com/map-lists-thumbnails/global-paleogeography-and-tectonics-in-deep-time/)

Bottke H (1965) Die exhalativ-sedimentären devonischen Roteisensteinlagertätten des Ostsauerlandes. Beih Geol Jahrb 63:1–147

Bottke H (1981) Lagerstättenkunde des Eisens: Geochemie, Genese, Typengliederung, wirtschaftliche Bedeutung. Verlag Glückauf, Essen, p 202p

Castendyk W (1855) Die Rotheisenstein-Lagerstätte der Grube Briloner Eisenberg bei Olsberg. Z Dtsch Geol Ges 7:253–260

Chan CS, McAllister SM, Leavitt AH, Glazer BT, Krepski ST, Emerson D (2016) The architecture of iron microbial mats reflects the adaptation of chemolithotrophic iron oxidation in freshwater and marine environments. Front Microbiol 7:796. https://doi.org/10.3389/fmicb.2016.00796

Cissarz A (1924) Mineralogisch-mikroskopische Untersuchungen der Erze und Nebengestein des Roteisensteinlagers der Grube Maria bei Braunfels an der Lahn. Mitt Kaiser-Wilhelm-Inst Eisenforschung 5:109–125

Cornell RM, Schwertmann U (2003) The iron oxides: structure, properties, reactions, occurrences, and uses, 2nd edn. Wiley-VCH, Weinheim, p 664p

Cruise MD (2000) Iron oxide and associated base metal mineralisation in the Central Midlands Basin, Ireland. PhD Thesis, Trinity College, Dublin, 479p

Davis CC, Chen H-W, Edwards M (2002) Modeling silica sorption to iron hydroxide. Environ Sci Technol 36:582–587. https://doi.org/10.1021/es010996t

Dengler H (1963) Befahrung der Roteisensteingrube Fortuna bei Berghausen (Lkrs. Wetzlar) der Harz-Lahn-Erzbergbau: am 8.1.1963, 4p

Di Bella M, Sabatino G, Quartieri S, Ferretti A, Cavalazzi B, Barbieri R, Foucher F, Messori F, Italiano F (2019) Modern iron ooids of hydrothermal origin as a proxy for ancient deposits. Sci Rep 9:7107. https://doi.org/10.1038/s41598-019-43181-y

Dimroth E, Lichtblau AP (1979) Metamorphic evolution of Archean hyaloclastites, Noranda area, Quebec, Canada. Part I: comparison of Archean and Cenozoic sea-floor metamorphism. Can J Earth Sci 16:1315–1340. https://doi.org/10.1139/e79-120

Dittmar D, Meyer W, Oncken O, Schievenbusch T, Walter R, von Winterfeld C (1994) Strain partitioning across a fold and thrust belt: the Rhenish Massif, Mid-European Variscides. J Struct Geol 16:1335–1352. https://doi.org/10.1016/0191-8141(94)90001-9

Dodd MS, Papineau D, Grenne T, Slack JF, Rittner M, Pirajno F, O'Neil J, Little CTS (2017) Evidence for early life in Earth's oldest hydrothermal vent precipitates. Nature 543:60–64. https://doi.org/10.1038/nature21377

Duhig NC, Stolz J, Davidson GJ, Large RR (1992) Cambrian microbial and silica gel textures in silica iron exhalites from the Mount Windsor Volcanic Belt, Australia: their petrography, chemistry, and origin. Econ Geol 87:764–784

Edwards KJ, Glazer BT, Rouxel OJ, Bach W, Emerson D, Davis RE, Toner BM, Chan CS, Tebo BM, Staudigel H, Moyer CL (2011) Ultra-diffuse hydrothermal venting supports Fe-oxidizing bacteria and massive umber deposition at 5000 m off Hawaii. ISME J 5:1748–1758

Egglseder MS, Cruden AR, Tomkins AG, Wilson SA, Langendam AD (2018) Colloidal origin of microbands in banded iron formations. Geochem Perspect Lett 6:43–49. https://doi.org/10.7185/geochemlet.1808

Elrick M, Gilleaudeau GJ, Romaniello SJ, Algeo TJ, Morford JL, Sabbatino M, Goepfert TJ, Cleal C, Cascales-Miñana B, Chernyavskiy P (2022) Major Early-Middle Devonian oceanic oxygenation linked to early land plant evolution detected using high-resolution U isotopes of marine limestones. Earth Planet Sci Lett 581:117410. https://doi.org/10.1016/j.epsl.2022.117410

Esposito V, Andaloro F, Canese S, Bortoluzzi G, Bo M, Di Bella M, Italiano F, Sabatino G, Battaglia P, Consoli P, Giordano P, Spagnoli F, La Cono V, Yakimov MM, Scotti G, Romeo T (2018) Exceptional discovery of a shallow-water hydrothermal site in the SW area of Basiluzzo islet (Aeolian archipelago, South Tyrrhenian Sea): an environment to preserve. PLoS One 13:1–27

Felgentreu C (2020) Lower Carboniferous hematitic cherts - a genetic link to the Middle/Upper Devonian jasper-rich iron ores of the Lahn-Dill type? Unpub Masters Thesis, Ruhr-Universität Bochum, 81p

Flaathen TK, Gislason SR, Oelkers EH, Sveinbjörnsdóttir ÁE (2009) Chemical evolution of the Mt. Hekla, Iceland, groundwaters: a natural analogue for CO2 sequestration in basaltic rocks. Appl Geochem 24:463–474. https://doi.org/10.1016/j.apgeochem.2008.12.031

Flick H, Nesbor HD, Behnisch R (1990) Iron ore of the Lahn-Dill type formed by diagenetic seeping of pyroclastic sequences - a case study on the Schalstein section at Gänsberg (Weilburg). Geol Rundsch 2:401–415. https://doi.org/10.1007/BF01830635

Franke W (1989) Variscan plate tectonics in Central Europe - current ideas and open questions. Tectonophysics 169:221–228. https://doi.org/10.1016/0040-1951(89)90088-7

Franke W, Cocks LRM, Torsvik TH (2017) The Palaeozoic Variscan oceans revisited. Gondwana Res 48:257–284. https://doi.org/10.1016/j.gr.2017.03.005

Franke W, Ballèvre M, Cocks L, Torsvik TH, Żelaźniewicz A (2021) Variscan Orogeny. In: Elias SA (ed) Encyclopedia of Geology, 2nd edn. Elsevier Science & Technology, San Diego, pp 338–349. https://doi.org/10.1016/B978-0-08-102908-4.00022-9

German CR, Seyfried WE Jr (2014) Hydrothermal processes. In: Mottl MJ, Elderfield H (eds) The oceans and marine geochemistry. Treatise on geochemistry, 2nd edn. Elsevier, Amsterdam, 8:191–233. https://doi.org/10.1016/B978-0-08-095975-7.00607-0

Gifkins CC, Allen RL (2001) Textural and chemical characteristics of diagenetic and hydrothermal alteration in glassy volcanic rocks: examples from the Mount Read Volcanics, Tasmania. Econ Geol 96:973–1002. https://doi.org/10.2113/gsecongeo.96.5.973

González FJ, Rincón-Tomás B, Somoza L, Santofimia E, Medialdea T, Madureira P, López-Pamo E, Hein JR, Marino E, Ignacio C de, Reyes J, Hoppert M, Reitner J (2020) Low-temperature, shallow-water hydrothermal vent mineralization following the recent submarine eruption of Tagoro volcano (El Hierro, Canary Islands). Mar Geol 430. https://doi.org/10.1016/j.margeo.2020.106333

Goodfellow WD (2007) Metallogeny of the Bathurst mining camp, northern New Brunswick. In: Goodfellow WD (ed) Mineral deposits of Canada: a synthesis of major deposit-types, district metallogeny, the evolution of geological provinces, and exploration methods. Geol Assoc Canada, Mineral Deposits Div, Spec Publ 5, pp 449–469

Gránásy L, Pusztai T, Tegze G, Warren JA, Douglas JF (2005) Growth and form of spherulites. Phys Rev E Stat Nonlin Soft Matter Phys 72:1–14. https://doi.org/10.1103/PhysRevE.72.011605

Grenne T, Slack JF (2003a) Bedded jaspers of the Ordovician Løkken ophiolite, Norway: seafloor deposition and diagenetic maturation of hydrothermal plume-derived silica-iron gels. Miner Deposita 38:625–639. https://doi.org/10.1007/s00126-003-0346-3

Grenne T, Slack JF (2003b) Paleozoic and Mesozoic silica-rich seawater: evidence from hematitic chert (jasper) deposits. Geology 31:319–322

Grenne T, Slack JF (2019) Mineralogy and geochemistry of silicate, sulfide, and oxide iron formations in Norway: evidence for fluctuating redox states of early Paleozoic marine basins. Miner Deposita 54:829–848. https://doi.org/10.1007/s00126-018-0840-2

Gross GA (1980) A classification of iron formations based on depositional environments. Can Mineral 18:215–222

Gudbrandsson S, Wolff-Boenisch D, Gislason SR, Oelkers EH (2011) An experimental study of crystalline basalt dissolution from 2 ≤ pH ≤ 11 and temperatures from 5 to 75 °C. Geochim Cosmochim Acta 75:5496–5509. https://doi.org/10.1016/j.gca.2011.06.035

Halama M, Swanner ED, Konhauser KO, Kappler A (2016) Evaluation of siderite and magnetite formation in BIFs by pressure-temperature experiments of Fe(III) minerals and microbial biomass. Earth Planet Sc Lett 450:243–253. https://doi.org/10.1016/j.epsl.2016.06.032

Harbort E (1903) Zur Frage nach der Entstehung gewisser devonischer Rotheisenerzlagerstätten. Neues Jb Mineral Geol Paleontol 1:179–192

Harder H (1954) Beitrag zur Petrographie und Genese der Hämatiterze des Lahn-Dill-Gebietes. Heidelb Beitr Mineral Petrographie 4:54–66

Heimann A, Johnson CM, Beard BL, Valley JW, Roden EE, Spicuzza MJ, Beukes NJ (2010) Fe, C, and O isotope compositions of banded iron formation carbonates demonstrate a major role for dissimilatory iron reduction in ~2.5 Ga marine environments. Earth Planet Sc Lett 294:8–18. https://doi.org/10.1016/j.epsl.2010.02.015

Hentschel H (1960) Zur Frage der Bildung der Eisenerze vom Lahn-Dill-Typ. Freib Forsch C 79:82–105

Hesemann J (1927) Die devonischen Eisenerze des Mittelharzes. Verlag von Wilhelm Knapp, Halle (Saale), p 54p

HLNUG (2007) Geologische Übersichtskarte von Hessen 1:300000. Hessisches Landesamt für Naturschutz, Umwelt und Geology, Wiesbaden

Hollis SP, Cooper MR, Herrington RJ, Roberts S, Earls G, Verbeeten A, Piercey SJ, Archibald SM (2015) Distribution, mineralogy and geochemistry of silica-iron exhalites and related rocks from the Tyrone Igneous Complex: Implications for VMS mineralization in Northern Ireland. J Geochem Explor 159:148–168. https://doi.org/10.1016/j.gexplo.2015.09.001

House M, Ziegler W (1977) The goniatite and conodont sequences in the early upper devonian at Adorf, Germany. Geol Palaeontol 11:69–108

Huber NK, Garrels RM (1953) Relation of pH and oxidation potential to sedimentary iron mineral formation. Econ Geol 48:337–357. https://doi.org/10.2113/gsecongeo.48.5.337

Huckriede H (1996) Lower Carboniferous stratiform iron-manganese mineralizations (Rheinisches Schiefergebirge, Germany): products of submarine hydrothermal activity and diagenetic manganese redistribution. Geol Mijnbouw 75:57–68

Iler RK (1979) The chemistry of silica: solubility, polymerization, colloid and surface properties, and biochemistry. Wiley, New York, p 866p

Jochum KP, Willbold M, Raczek I, Stoll B, Herwig K (2005) Chemical characterisation of the USGS reference glasses GSA-1G, GSC-1G, GSD-1G, GSE-1G, BCR-2G, BHVO-2G and BIR-1G using EPMA, ID-TIMS, ID-ICP-MS and LA-ICP-MS. Geostand Geoanal Res 29:285–302. https://doi.org/10.1111/j.1751-908X.2005.tb00901.x

Jorge R, Relvas J, Barriga F (2005) Silica gel microtextures in siliceous exhalites at the Soloviejo manganese deposit, Spain. 8th SGA Biennial Meeting, Beijing, China, Society for Geology applied to Mineral Deposits 631–634. https://doi.org/10.1007/3-540-27946-6_161

Kastner M, Keene JB, Gieskes JM (1977) Diagenesis of siliceous oozes—I. Chemical controls on the rate of opal-A to opal-CT transformation—an experimental study. Geochim Cosmochim Acta 41:1041–1059. https://doi.org/10.1016/0016-7037(77)90099-0

Kegel W (1922) Abriß der Geologie der Lahnmulde. Erläuterungen zu einer von Johannes Ahlburg hinterlassenen Übersichtskarte und Profildarstellung der Lahnmulde. Abh Preuss Geol Landesanst 86:1–81

Kendall B, Anbar AD, Kappler A, Konhauser KO (2012) The global iron cycle. In: Knoll AH, Canfield DE, Konhauser KO (eds) Fundamentals of geobiology. John Wiley & Sons, Hoboken, New Jersey, pp 65–92

Kimberley MM (1989) Nomenclature for iron formations. Ore Geol Rev 5:1–12. https://doi.org/10.1016/0169-1368(89)90002-4

Kirnbauer T (1998) Alpinotype Zerrklüfte. In: Kirnbauer T (ed) Geologie und hydrothermale Mineralisationen im rechtsrheinischen Schiefergebirge. Nassauischer Verein für Naturkunde, pp 150–156

Köhler I, Konhauser KO, Papineau D, Bekker A, Kappler A (2013) Biological carbon precursor to diagenetic siderite with spherical structures in iron formations. Nat Commun 4:1–7. https://doi.org/10.1038/ncomms2770

Konhauser KO, Planavsky NJ, Hardisty DS, Robbins LJ, Warchola TJ, Haugaard R, Lalonde SV, Partin CA, Oonk P, Tsikos H, Lyons TW, Bekker A, Johnson CM (2017) Iron formations: a global record of Neoarchaean to Palaeoproterozoic environmental history. Earth-Sci Rev 172:140–177. https://doi.org/10.1016/j.earscirev.2017.06.012

Kräutner HG (1977) Hydrothermal-sedimentary iron ores related to submarine volcanic rises: the Teliuc-Ghelar type as a carbonatic equivalent of the Lahn-Dill type. In: Klemm DD, Schneider H-J (eds) Time- and stratabound ore deposits. Springer, Berlin, pp 232–253

Krebs W (1960) Stratigraphie, Vulkanismus und Fazies des Oberdevons zwischen Donsbach und Hirzenheim (Rheinisches Schiefergebirge, Dill-Mulde). Abh Hessischen Landesamtes Bodenforschung 33:1–119

Kretschmer (1899) Die Eisenerzlagerstätten des mährischen Devon. Jahrb Geol Reichsanst 49:29–124

Kruber C, Thorseth IH, Pedersen RB (2008) Seafloor alteration of basaltic glass: textures, geochemistry, and endolithic microorganisms. Geochem Geophys Geosyst 9:1–18. https://doi.org/10.1029/2008GC002119

Kruhl JH, Peternell M (2002) The equilibration of high-angle grain boundaries in dynamically recrystallized quartz: the effect of crystallography and temperature. J Struct Geol 24:1125–1137. https://doi.org/10.1016/S0191-8141(01)00096-7

Kruhl JH, Wirth R, Morales LFG (2013) Quartz grain boundaries as fluid pathways in metamorphic rocks. J Geophys Res 118:1957–1967. https://doi.org/10.1002/jgrb.50099

Leistel JM, Marcoux E, Deschamps Y (1997) Chert in the iberian pyrite belt. Miner Deposita 33:59–81. https://doi.org/10.1007/s001260050133

Lippert HJ (1951) Zur Gesteins- und Lagerstättenbildung in Roteisenstein-Gruben des östlichen Dill-Gebietes. Abh Senckenb Naturforsch Ges 485:1–29

Lippert HJ (1953) Das Roteisenstein-Grenzlager von der Wende Mittel-Oberdevon in der Dill-Mulde: Beobachtungen und Gedanken zur Entstehung von Erz und Nebengestein. Z Dtsch Geol Ges 1953:259–276

Lippert HJ (1997) Eisenerze. In: Bender P, Lippert HJ, Nesbor HD (eds) Geologische Karte von Hessen, Blatt 5216 Oberscheld. Hessisches Landesamt für Bodenforschung, Wiesbaden, pp 236–291

Lippert HJ (1970) Roteisenstein-Grenzlager. In: Lippert HJ, Hentschel H, Rabien A (eds) Geologische Karte von Hessen, Blatt 5215 Dillenburg. Hessisches Landesamt für Bodenforschung, pp 410–422

Lippert HJ, Flick H (1998) Vulkano-sedimentare Roteisenerze vom Lahn-Dill-Typ. In: Kirnbauer T (ed) Geologie und hydrothermale Mineralisationen im rechtsrheinischen Schiefergebirge. Nassauischer Verein für Naturkunde, pp 121–129

Little CTS, Johannessen KC, Bengtson S, Chan CS, Ivarsson M, Slack JF, Broman C, Thorseth IH, Grenne T, Rouxel OJ, Bekker A (2021) A late Paleoproterozoic (1.74 Ga) deep-sea, low-temperature, iron-oxidizing microbial hydrothermal vent community from Arizona, USA. Geobiology 19:228–249. https://doi.org/10.1111/gbi.12434

Luhmann AJ, Tutolo BM, Tan C, Moskowitz BM, Saar MO, Seyfried WE (2017) Whole rock basalt alteration from CO_2-rich brine during flow-through experiments at 150 °C and 150 bar. Chem Geol 453:92–110. https://doi.org/10.1016/j.chemgeo.2017.02.002

May A (1987) Der Massenkalk (Devon) nördlich von Brilon (Sauerland). Geol Paläontol Westfalen 10:51–84

McMahon S (2019) Earth's earliest and deepest purported fossils may be iron-mineralized chemical gardens. Proc Biol Sci 286:1–9. https://doi.org/10.1098/rspb.2019.2410

Meisl S (1970) Petrographische Studien im Grenzbereich Diagenese-Metamorphose. Abh Hessischen Landesamtes Bodenforschung 57:1–93

Melián G, Hernández PA, Padrón E, Pérez NM, Barrancos J, Padilla G, Dionis S, Rodríguez F, Calvo D, Nolasco D (2014) Spatial and temporal variations of diffuse CO_2 degassing at El Hierro volcanic system: relation to the 2011–2012 submarine eruption. J Geophys Res 119:6976–6991. https://doi.org/10.1002/2014JB011013

Murata KJ, Larson RR (1975) Diagenesis of Miocene siliceous shales, Temblor Range, California. J Res US Geol 3:553–566

Nakamura K, Kato Y (2004) Carbonatization of oceanic crust by the seafloor hydrothermal activity and its significance as a CO_2 sink in the Early Archean. Geochim Cosmochim Acta 68:4595–4618. https://doi.org/10.1016/j.gca.2004.05.023

Nesbor H-D (2004) Paläozoischer Intraplattenvulkanismus im östlichen Rheinischen Schiefergebirge – Magmenentwicklung und zeitlicher Ablauf. Geol Jahrb Hess 131:145–182

Nesbor H-D, Buggisch W, Flick H, Horn M, Lippert HJ (1993) Vulkanismus im Devon des Rhenoherzynikums: Fazielle und paläogeographische Entwicklung vulkanisch geprägter mariner Becken am Bespiel des Lahn- Dill-Gebietes. Geol Abh Hess 98:3–87

Paeckelmann W (1936) Erläuterungen zu Blatt 4617 Brilon. Preussisches Geologisches Landesanstalt, Berlin, p 65p

Palinkaš LA, Šoštarić SB, Palinkaš SS (2008) Metallogeny of the Northwestern and Central Dinarides and Southern Tisia. Ore Geol Rev 34:501–520. https://doi.org/10.1016/j.oregeorev.2008.05.006

Papineau D, She Z, Dodd MS, Iacoviello F, Slack JF, Hauri E, Shearing P, Little CTS (2022) Metabolically diverse primordial microbial communities in Earth's oldest seafloor-hydrothermal jasper. Sci Adv 8:eabm2296. https://doi.org/10.1126/sciadv.abm2296

Petránek J, van Houten F (1997) Phanerozoic ooidal ironstones: contribution to the International Geological Correlation Programme, Project 277 - Phanerozoic ooidal ironstones, 1st edn. Czech Geological Survey special papers, vol 7. Czech Geological Survey, Prague

Putnis A (2002) Mineral replacement reactions: from macroscopic observations to microscopic mechanisms. Mineral Mag 66:689–708. https://doi.org/10.1180/0026461026650056

Quade H (1968) Die Entwicklung des initialen Geosynklinalmagmatismus und die Bildung der exhalativ-sedimentären Eisenerzlagerstätten im mitteleuropäischen Variszikum. Universität Clausthal, Habilitationsschrift, p 278p

Quade H (1969) Die Roteisensteingrube Fortuna bei Berghausen. Wetzlar, Universität Clausthal, Krs, p 30p

Quade H, Nyk R, Walde R (1981) Überschiebungstektonik in der Eisenerzlagerstätte Fortuna bei Berghausen/Dill (Rheinisches Schiefergebirge). Z Dtsch Geol Ges 132:29–41

Radvanec M, Grecula P (2016) Geotectonic and metallogenic evolution of Gemericum (Inner Western Carpathians) from Ordovician to Jurassic. Mineral Slovaca 48:105–118

Roemer F (1844) Das Rheinische Uebergangsgebirge. Hahn'sche Hofbuchhandlung, Hannover, 96p

Rösler HJ (1962) Zur Entstehung der oberdevonischen Eisenerze vom Typ Lahn-Dill in Ostthüringen. Freib Forsch C138:1–79

Saffarini G (1982) Geochemisch-statistische Untersuchungen an Eisenerz- und Nebengesteinsserien der Lagerstätte Fortuna bei Berghausen/Dill. Dissertation, Universität Clausthal, 195p

Sandberger F (1847) Übersicht über die geologischen Verhältnisse des Herzogthums Nassau. Verlag von Christian Wilhelm Kreidel, Wiesbaden, p 401p

Sangster DF (2001) The role of dense brines in the formation of vent-distal sedimentary-exhalative (SEDEX) lead–zinc deposits: field and laboratory evidence. Miner Deposita 37:149–157. https://doi.org/10.1007/s00126-001-0216-9

Schaeffer R (1980) Vulkanogen-sedimentäre Manganerzlager im Unterkarbon bei Laisa (Dillmulde, Rheinisches Schiefergebirge). Geol Jahrb Hess 108:151–170

Schmitt L, Kirnbauer T, Angerer T, Kraemer D, Garbe-Schoenberg D, Fockenberg T, Klein S (n.d.) Genesis of Devonian volcanic-associated Lahn-Dill-type iron ores – part II: trace element fractionation mechanisms as evidence for diffuse fluid venting, submitted to Miner Deposita

Scholten JC, Scott SD, Garbe-Schönberg D, Fietzke J, Blanz T, Kennedy CB (2004) Hydrothermal iron and manganese crusts from the Pitcairn Hotspot Region. In: Hekinian R, Cheminée J-L, Stoffers P (eds) Oceanic hotspots: intraplate submarine magmatism and tectonism. Springer, Heidelberg, pp 375–405

Schultz RW (1966) Lower Carboniferous cherty ironstones at Tynagh, Ireland. Econ Geol 61:311–342. https://doi.org/10.2113/gsecongeo.61.2.311

Schwertmann U, Friedel J, Stanjek H (1999) From Fe(III) ions to ferrihydrite and then to hematite. J Colloid Interf Sci 209:215–223. https://doi.org/10.1006/jcis.1998.5899

Seyfried WE Jr, Mottl MJ (1982) Hydrothermal alteration of basalt by seawater under seawater-dominated conditions. Geochim Cosmochim Acta 46:985–1002. https://doi.org/10.1016/0016-7037(82)90054-0

Sherrell RM, Field M, Ravizza G (1999) Uptake and fractionation of rare earth elements on hydrothermal plume particles at 9°45′N, East Pacific Rise. Geochim Cosmochim Acta 63:1709–1722. https://doi.org/10.1016/S0016-7037(99)00182-9

Skulski T, Castonguay S, van Staal C, Rogers N, McNicoll V, Kerr A, Escayola M (2009) Baie Verte Peninsula: an evolving geological story. Annual Fall Field Trip 2009, Geological Association of Canadan Newfoundland and Labrador Section, pp 1–76

Stets J, Schäfer A (2002) Depositional environments in the lower Devonian siliciclastics of the Rhenohercynian Basin (Rheinisches Schiefergebirge, W-Germany): Case Studies and a Model. Schweizerbart, Stuttgart, p 73p

Stranghoener M, Dultz S, Behrens H, Schippers A (2020) Potential mobilizable Fe from secondary phases of differentially altered subsurface basaltic rock - a sequential extraction study on ICDP site Hawaii. Appl Geochem 121:104705. https://doi.org/10.1016/j.apgeochem.2020.104705

Vernon RH (1976) Deformation, recovery and recrystallisation processes. In: Vernon RH (ed) Metamorphic processes: reactions and microstructure development. Springer, Dordrecht, pp 148–172

von Damm KL (1995) Controls on the chemistry and temporal variability of seafloor hydrothermal fluids. In: Humphris S (ed) Seafloor hydrothermal systems: physical, chemical, biological, and geological interactions, 1st edn. American Geophysical Union, Washington, pp 222–247

von Gümbel CW (1879) Geognostische Beschreibung des Fichtelgebirges mit dem Frankenwald und dem westlichen Vogtlande. Justus Perthes, Gotha, 658p

Weber L (1997) Handbuch der Lagerstätten der Erze, Industrieminerale und Energierohstoffe Österreichs: Erläuterungen zur Metallogenetischen Karte Österreichs. Archiv für Lagerstättenforschung der Geologischen Bundesanstalt, 545p

Whitney DL, Evans BW (2010) Abbreviations for names of rock-forming minerals. Am Mineral 95:185–187. https://doi.org/10.2138/am.2010.3371

Williams LA, Crerar DA (1985) Silica diagenesis, II. General mechanisms. J Sediment Petrol 55:312–321

Winchester JA, Floyd PA (1977) Geochemical discrimination of different magma series and their differentiation products using immobile elements. Chem Geol 20:325–343. https://doi.org/10.1016/0009-2541(77)90057-2